AGU PUBLICATIONS

Geochemistry, Geophysics, Geosystems

RESEARCH ARTICLE
10.1002/2014GC005617

Special Section:
The Lithosphere-Asthenosphere System

Key Points:
- We map variations in lithospheric structure across Continental Borderland
- Structure of Outer Borderland lithosphere rules out substantial extension
- Lithospheric thickness of young Pacific plate indicates weak age-dependence

Correspondence to:
V. Lekić,
ved@umd.edu

Citation:
Reeves, Z., V. Lekić, N. Schmerr, M. Kohler, and D. Weeraratne (2015), Lithospheric structure across the California Continental Borderland from receiver functions, *Geochem. Geophys. Geosyst.*, *16*, 246–266, doi:10.1002/2014GC005617.

Received 13 OCT 2014
Accepted 1 JAN 2015
Accepted article online 8 JAN 2015
Published online 30 JAN 2015

Lithospheric structure across the California Continental Borderland from receiver functions

Zachary Reeves[1], Vedran Lekić[1], Nicholas Schmerr[1], Monica Kohler[2], and Dayanthie Weeraratne[3]

[1]Department of Geology, University of Maryland, College Park, Maryland, USA, [2]Department of Mechanical and Civil Engineering, California Institute of Technology, Pasadena, California, USA, [3]Department of Geological Sciences, California State University, Northridge, California, USA

Abstract Due to its complex history of deformation, the California Continental Borderland provides an interesting geological setting for studying how the oceanic and continental lithosphere responds to deformation. We map variations in present-day lithospheric structure across the region using Ps and Sp receiver functions at permanent stations of the Southern California Seismic Network as well as ocean bottom seismometer (OBS) data gathered by the Asthenospheric and Lithospheric Broadband Architecture from the California Offshore Region Experiment (ALBACORE), which enhances coverage of the borderland and provides first direct constraints on the structure of the Pacific plate west of the Patton Escarpment. Noisiness of OBS data makes strict handpicking and bandpass filtering necessary in order to obtain interpretable receiver functions. Using H-κ and common-conversion point stacking, we find pronounced lithospheric differences across structural blocks, which we interpret as indicating that the Outer Borderland has been translated with little to no internal deformation, while the Inner Borderland underwent significant lithospheric thinning, most likely related to accommodating the 90° clockwise rotation of the Western Transverse Range block. West of the Patton Escarpment, we find that the transition to typical oceanic crustal thickness takes place over a lateral distance of ~ 50 km. We detect an oceanic seismic lithosphere-asthenosphere transition at 58 km depth west of the Patton Escarpment, consistent with only weak age-dependence of the depth to the seismic lithosphere-asthenosphere transition. Sp common-conversion point stacks confirm wholesale lithospheric thinning of the Inner Borderland and suggest the presence of a slab fragment beneath the Outer Borderland.

1. Introduction

The Continental Borderland is arguably one of the most geologically unusual regions in the United States because of its history of deformation involving subduction, transtensional, and transpressional motion, as well as extension. The term Continental Borderland is applied to the region off the southwestern coast of California that spans from ~32° to ~34° N and from the coast of California to 121° W (see Figure 1). This area coincides with the tectonic plate boundary between the North American and Pacific plates.

Structurally, the Continental Borderland is characterized by basins and ranges that run generally parallel to the coastline (striking northwest), with the islands denoting local peaks of the ranges and the bathymetric lows corresponding to the basins [*Junger*, 1976]. Lithologically, the region bears widespread evidence of the subduction zone that existed between the Farallon plate and North American plate. The Outer Borderland consists primarily of the Franciscan Belt subduction complex, and the Great Valley Belt forearc basin deposit [*Crouch*, 1979]. Seismic studies and offshore drilling detect mafic basement underlying these younger formations [*Bohannon and Geist*, 1998; *ten Brink et al*., 2000]. The Great Valley Belts observed in the Western Transverse Ranges (WTR), Inner Borderland, and Outer Borderland have undergone very slight metamorphism and deformation and are inferred to derive from a continental source terrane [*Crouch*, 1979]. Within the Inner Borderland, Santa Catalina Island represents an unroofed metamorphic core complex, where the Catalina Schist is exposed at the surface. The Catalina Schist primarily contains blueschist facies, a relatively high-pressure and low-temperature metamorphic grade typically present within subduction zones, though the Catalina schist also has some higher-temperature lithologies [*Grove et al*., 2008].

Structural, petrological, and paleomagnetic data are primary constraints for reconstructions of deformation history in the Continental Borderland. Deformation has been governed by the transition from compression

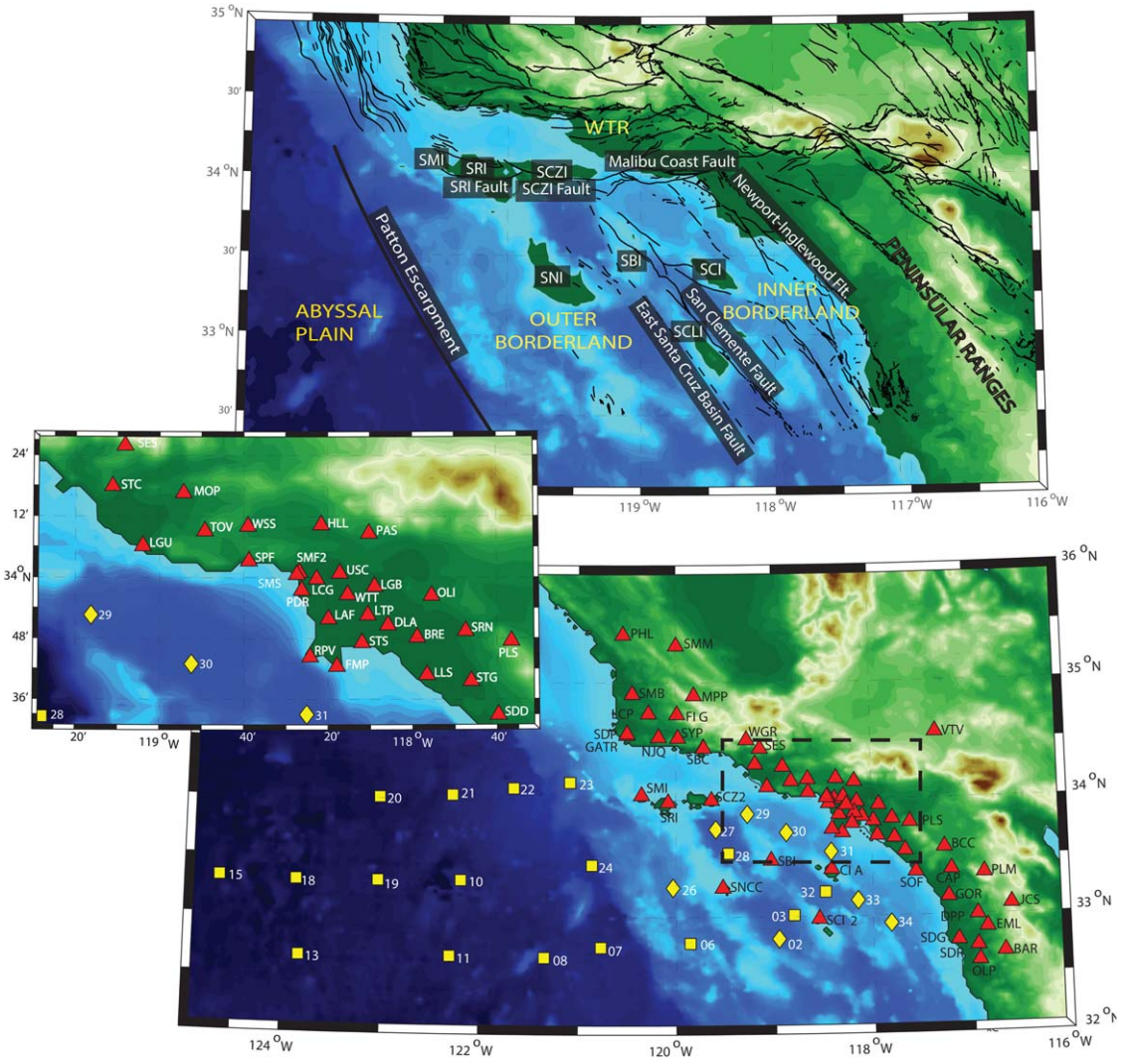

Figure 1. (top) Map of study region showing the main faults and structural blocks. Faults are from the Southern California Earthquake Center (www.scec.org) database, except for the East Santa Cruz Basin Fault, which is from *Howell et al*. [1976]. (WTR—Western Transverse Range block, SMI—San Miguel Island, SRI—Santa Rosa Island, SCZI—Santa Cruz Island, SNI—San Nicolas Island, SBI—Santa Barbara Island, SCI—Santa Catalina Island, SCLI—San Clemente Island, SRI Fault—Santa Rosa Island Fault, SCZI Fault—Santa Cruz Island Fault). (bottom) Map of locations of the ALBACORE (yellow) long-period (squares) and short-period (diamonds) deployment as well as the Southern California Seismic Network (CI, red triangles) used in this study. Stations at which no seismometer data were recovered are not shown. The inset (middle) corresponds to the Los Angeles area (black square). The darker blues are more negative elevations (deeper water), and light greens and browns are higher elevations relative to sea level.

to transform motion following cessation of subduction ~30 Ma. Paleomagnetic data from volcanic rocks across the WTR bear evidence of multiple instances of block rotation together accounting for a total of ~90° clockwise rotation [*Kamerling and Luyendyk*, 1979; *Carter et al*., 1987; *Luyendyk*, 1991; *Luyendyk et al*., 1980; *Crouch and Suppe*, 1993] of the WTR block. *Nicholson et al*. [1994] gives a compelling argument for the importance of microplate formation and capture in causing the large clockwise rotation of the WTR (Figure 2): after the Monterey microplate was captured, the WTR block began to rotate as it was subjected to dextral shear on the eastern boundary and sinistral shear on the southern boundary, with the block's northern region being coupled to the North American plate. In this model, the WTR block rode atop the part of the Monterey microplate that was captured by the Pacific plate.

The fact that Catalina Schist is exposed throughout the Inner Borderland is interpreted as removal of a large amount (~40 km) of overburden. *Crouch and Suppe* [1993] propose that the overburden was removed through rifting that occurred in the wake of the rotation of the WTR (see Figure 2). However, the total extension of 200–250 km across the 100 km wide Inner Borderland advanced by *Crouch and Suppe* [1993] is

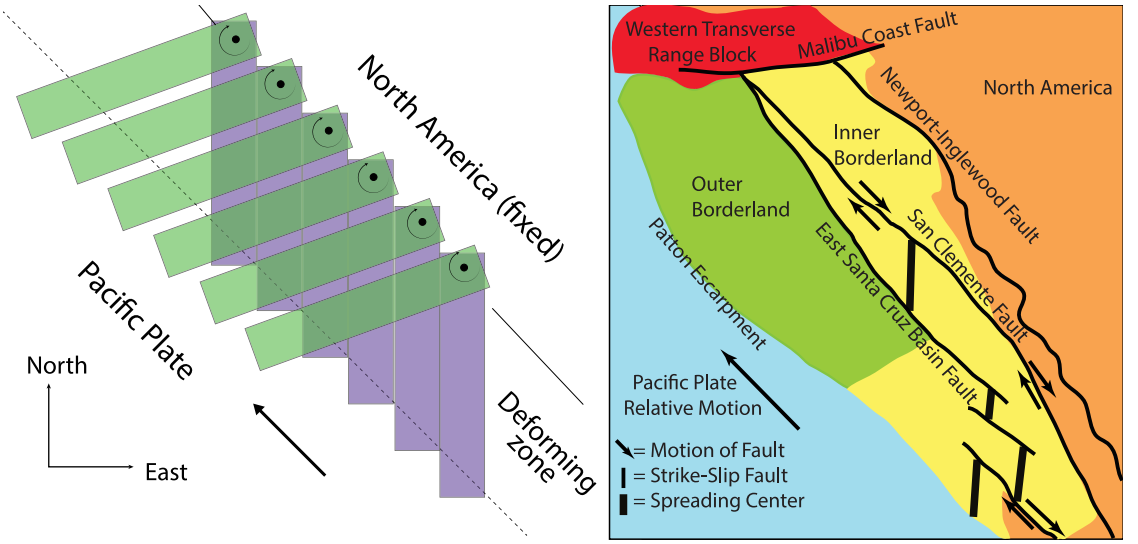

Figure 2. (left) The *Luyendyk et al*. [1980] and *Luyendyk* [1991] model for the WTR block rotation where blocks rotated together, with relatively little extension occurring in the present-day Inner Borderland. The green rectangles are the blocks post rotation with the spaces representing detachment faulting between blocks. (right) The *Crouch and Suppe* [1993] model where substantial rifting of the Inner Borderland accompanied the rotation of the WTR block. The spreading centers accommodate the rotation of the Western Transverse Range block in this model.

larger by a factor of two than the extension inferred in later studies based on multichannel, seismic reflection studies of the upper crust [*Bohannon and Geist*, 1998]. Geophysical observations by *ten Brink et al*. [2000], including gravity and wide-angle seismic refraction data, across the Inner Borderland also support substantial extension across the region, enabled in part by temporary mantle upwelling that accompanied the rotation of the WTR. An alternate scenario, proposed by *Luyendyk et al*. [1980] and *Luyendyk* [1991] is that rotation of the WTR was accompanied by rotation of other blocks, which resulted in highly localized extension forming the Catalina and Los Angeles basins, but did not result in wholesale lithospheric extension (Figure 2).

The Outer Borderland is thought to have translated away from the North America plate before being captured by the Pacific plate ~18 Mya [*Nicholson et al*., 1994]. Furthermore, this translation was not accompanied by substantial block rotation, since structural blocks north of the Outer Borderland, which already took on the same motion as the Pacific plate, could not serve as a "hinge" akin to the one enabling rotation of the WTR.

This and other [e.g., *Atwater and Stock*, 1998; *McQuarrie and Wernicke*, 2005] reconstructions of the structural evolution in the region are based on geographically spotty constraints from geology, paleomagnetism, mineralogy, petrology, geochronology, and fault slip interfaces. Here we investigate whether present-day lithospheric structure across the Continental Borderland bears evidence of this complex deformational history. We seek to identify the seismic signature of the lithosphere across different structural blocks. Specifically, we examine the hypothesis that the crust and mantle lithosphere of the Outer Borderland is substantially thicker than the thinned lithosphere found beneath the Inner Borderland [e.g., *ten Brink et al*., 2000]. We also investigate whether or not the Outer Borderland bears a structural similarity to the crust beneath coastal stations in southernmost California from where the block is thought to have originated. Finally, we assess how the transition between the Outer Borderland and the Pacific plate to the west of the Patton Escarpment manifests in the structure of the crustal and mantle lithosphere.

2. Data and Noise

To examine the crust and mantle underlying our study region, we used three-component, broadband data recorded by 61 stations of the Southern California Seismic Network, as well as data from 25 ocean bottom seismometers (OBS) deployed as part of the Asthenospheric and Lithospheric Broadband Architecture from

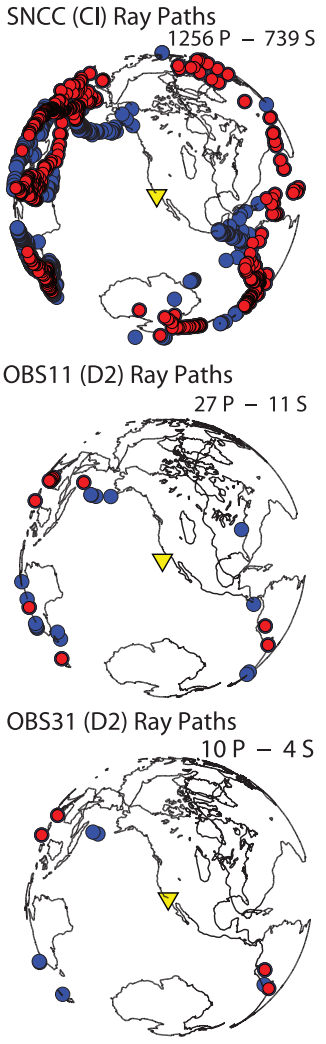

Figure 3. Sources of earthquakes for stations SNCC (top), OBS11 (middle), and OBS31 (bottom). Blue circles are the earthquakes used in Ps computations. Red circles are earthquakes used in Sp and Ps computations. Yellow triangles are the stations.

the California Offshore Region Experiment [ALBACORE: *Kohler and Science Party*, 2010, 2011] in 2010–2011 (Figure 1). The ALBACORE data enhance coverage of the borderland and provide the first direct constraints on the structure of the Pacific plate west of the Patton Escarpment.

To minimize contamination from upper mantle triplications and core-reflected phases, we analyzed P-to-S waveforms from events with epicentral distances ranging from 30° to 90° (blue circles in Figure 3). T For Sp, the optimal epicentral distance for earthquakes is between 60° and 75° and centroid depth less than 300 km. This is because S-to-P waveforms from deeper or more distant earthquakes are contaminated by ScS and SKS (core phases) and P waves that have reflected multiple times off of the surface [*Wilson et al*., 2006]. At ocean-bottom stations, we expand the allowed epicentral distance range, this time to 55°–85° (red circles in Figure 3) in order to include more data; because this introduces contamination in the Sp receiver functions for deeper structure, we restrict their interpretation to the upper 100 km. Even with this broader epicentral distance range, the short duration of the ALBACORE deployment resulted in very few (typically a dozen or so) usable Sp waveforms (Figure 3). For both PS and Sp, we limited our analysis to earthquakes with a minimum moment magnitude of 5.8 as smaller events did not produce a signal-to-noise ratio (as measured by the algorithm of *Abt et al*. [2010]) high enough to make reliable interpretations.

The receiver function method relies on high-quality recordings of the P wave and its coda, as well as those of the S wave and its precursors. Thus, we hand-pick all the data available from the ALBACORE deployment and retain only those seismograms on which the P and S arrivals are both clear, and background noise level observed before the P arrival is small (signal-to-noise ratio $> \sim 2$). To further reduce the effects of noise in the ocean-bottom environment, we bandpass-filter the data to the 0.03–0.12 Hz frequency range (see Discussion section). At ALBACORE stations, we obtained data for 3577 waveforms pairs, where a waveform pair is defined as 1 earthquake detected at 1 station; After hand-picking, we retained 327 pairs (∼9%). The fraction of usable data was much lower at the short-period ocean bottom stations (diamonds in Figure 1) than at the broadband stations (squares in Figure 1).

The main reasons for data rejection at OBS stations included seismometer malfunction, noise, or overprinting of signal by sedimentary multiples. The distribution of handpicked waveforms with high signal to noise ratios (>2) is not identical from station to station and the actual events selected for our data set at each station are not necessarily the same. In general, the OBS stations west of the Patton Escarpment tended to have more waveforms with high signal to noise ratios than the events in, or on the fringe of the California Borderland. The broadband seismic stations have more usable events than the short-period stations because these long-period stations are more effective at recording low frequencies, suggesting that the signal to noise ratios decrease at shorter periods.

The benefit of handpicking the data can be seen in Figure 4, where Figure 4a shows a Ps receiver function single-station stack for OBS11 in the abyssal plain obtained after handpicking only high-quality events; Figure 4c shows the Ps receiver function single-station stack from the same station with all of the data OBS11 recorded. Figures 4b and d show the Ps receiver functions in 11 epicentral distance bins. The quality

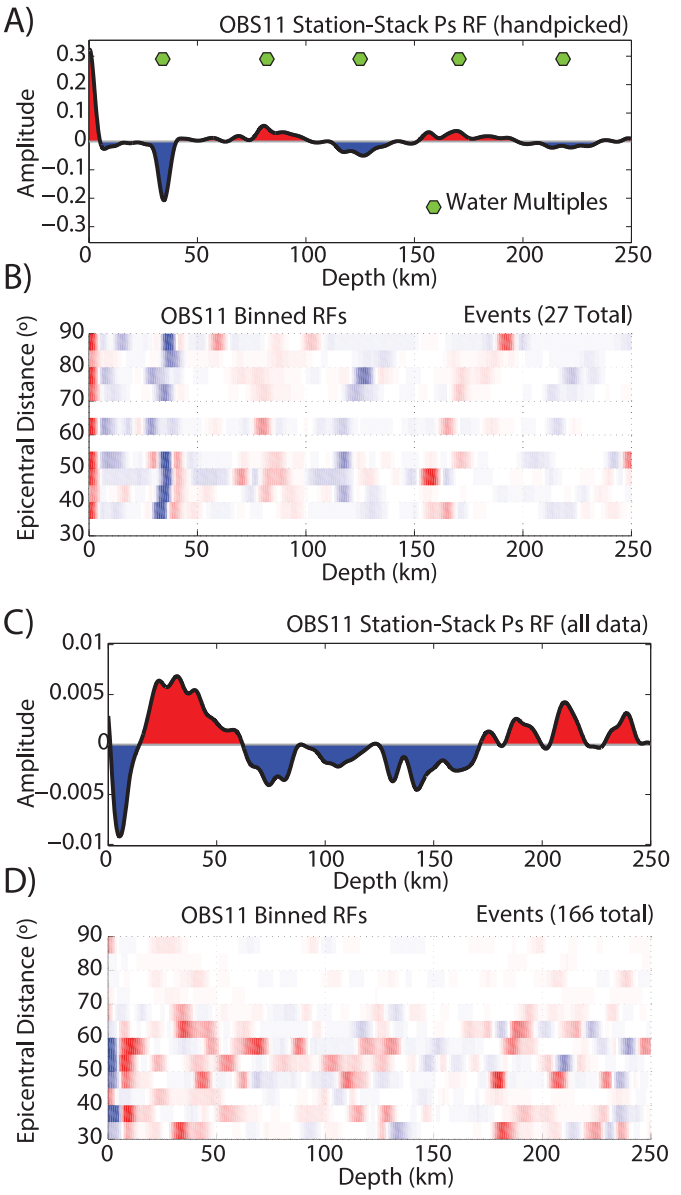

Figure 4. (a) Ps receiver function single-station stack for ALBACORE station OBS11 in the abyssal plain obtained after handpicking only high-quality events, with water multiples evident (green hexagons). (b) Ps receiver functions obtained from hand-picked data binned in 11 epicentral distance bins. (c) Ps receiver function single-station stack for OBS11 obtained from all available events. (d) Ps receiver functions obtained from all available data binned in 11 epicentral distance bins. Note that hand-picking results in substantially higher signal-to-noise ratios and clear Ps signals. Both receiver functions are constructed from data that has been bandpass filtered from .03 to .12 Hz.

difference is substantial, and clear water multiples can be seen in the handpicked data, whereas coherency of the result is much lower in the data that are not handpicked. The flip side of handpicking high signal-to-noise data (versus processing all the data) from a short deployment is that at many of the ocean bottom seismic stations, only a handful of waveforms remain for which to calculate receiver functions (as few as 1). Therefore, although handpicking allows us to obtain estimates of crustal and lithospheric structure in the first place, these estimates have relatively high uncertainty compared to constraints from permanent land stations with more abundant data.

Data were also requested for the permanent seismic network stations on the seven islands in the region, as well as 54 stations along the coastline, L.A. Basin, Peninsular Ranges, Western Transverse Range block, and one inland station (VTV) in Victorville, CA that is known to be high quality to serve as a reference station (triangles in Figure 1). These stations are part of the permanent Southern California Seismic Network (SCSN, www.data.scec.org/station/index.html). At these stations, we use the traditional band-pass of 0.5–0.03 Hz for the Ps and 0.25–0.03 Hz for the Sp waveforms. Both Ps and Sp waveforms recorded by these stations are more abundant and higher quality than the ALBACORE data. For example, there were 294 waveforms handpicked from the seven island stations (average 42/station) during the same timeframe as the ALBACORE project, for which there were 327 waveforms handpicked from 22 long-period ocean bottom stations (average of 14.9/station). In total, we obtained waveform data from 68,357 station-event pairs at SCSN land/island stations.

The biggest earthquake occurring during the time of the ALBACORE deployment was the $M_W \sim 9.0$ [*Ammon et al.*, 2011] Tohoku earthquake of 11 March 2011. Unfortunately, this event's numerous aftershocks made receiver-function analysis of the waveforms challenging, thus rendering a substantial fraction of waveforms recorded by ALBACORE unusable.

3. Methods

3.1. Receiver Functions

We apply the receiver function method to constrain variations in lithospheric structure since it can achieve both high vertical and horizontal resolution estimates for the depth of lithospheric velocity interfaces. The receiver function method relies upon detecting and analyzing conversions of P waves to S waves (and vice versa), and is useful in characterizing impedance contrasts (e.g., Moho or seismic lithosphere-asthenosphere transition) in the subsurface [*Langston*, 1977]. The differences in relative arrival times between the parent and converted waves can be used to constrain the interface depths and average velocities between interfaces, while the amplitudes of the converted waves relative to the parent waves carry information about the strength and polarity of the impedance contrast.

Throughout our study, we use Ps (P is parent, S is daughter) to constrain variations in Moho depth, as Ps waveforms have much higher signal-to-noise levels compared to Sp, which are not only contaminated by microseismic noise [e.g., *Kolb and Lekic*, 2014], but also have an inherently longer-period signal content. For deeper interfaces, such as the lithosphere-asthenosphere transition (LAT), we use Sp as Ps waves converted across deeper structures are often overprinted by crustal multiples. Because Sp signals from deep structures always reach the seismometer before conversions across shallower structures and before the direct S-wave, Sp receiver functions are particularly well suited for studying deep lithospheric structure.

To suppress source-side waveform complexity and isolate interpretable receiver functions (RF), we deconvolve the parent wave from the daughter wave in the time and/or frequency domains. We obtained clearest RFs when we performed the Sp deconvolution in the frequency domain and the Ps deconvolution in the time domain. To stabilize the frequency-domain deconvolution of Sp, we use a water level damping; this encompasses adding a positive constant to eliminate spectral holes or frequencies at which there would be a division by 0 to the power spectrum of the parent waveform. The water level damping constant was allowed to vary by several orders of magnitude with respect to the optimal level obtained using the method of *Abt et al.* [2010]. It is important to note that even with the use of the water level, it can be difficult to obtain reliable receiver functions from single-parent-daughter waveform pairs in the presence of high noise levels, which are characteristic of Sp waveforms. Therefore, while we use damped spectral division and simultaneously deconvolve all waveform pairs at a station [e.g., *Bostock*, 1998], we also calculated Sp receiver functions for individual parent-daughter pairs using a version of the extended time multitaper method [*Helffrich*, 2006; *Lekic and Fischer*, 2013]. The time domain deconvolution is performed using an iterative procedure based on *Ligorría and Ammon* [1999].

3.2. Depth to and Average $\frac{V_P}{V_S}$ Above Subsurface Interfaces

In order to translate the receiver functions from a function of (lag)time to constraints on the depths of structural interfaces such as the Moho, we need a velocity model for the subsurface that specifies both shear V_S and compressional V_P wave speeds. The lag time between the arrival of the parent and daughter waves is a function of three structural parameters: (1) the compressional wave speed (V_P), (2) the $\frac{V_P}{V_S}$ ratio (κ), and (3) the depth (H) to the discontinuity across which the conversion(s) occurred. Trade-offs between κ and H, and to a lesser extent V_P mean that the lag times associated with strong phases in a receiver function cannot by themselves simultaneously constrain all three of these parameters. This is because there is an infinite number of combinations of the three parameters that could produce the same difference in arrival time between the P and S waves. Fortunately, converted waves that bounce within crustal layers—PpPs, PsPs, and PpSs—depend on the V_P, κ, and H in different ways. Therefore, when multiple phases are analyzed simultaneously, these trade-offs can be reduced.

We use H-κ stacking of Ps receiver functions [*Zhu and Kanamori*, 2000] to combine the constraints from direct conversions and those from multiple-bounce converted waves. In this procedure, lag times of the Ps, PpPs, PsPs, and PpSs are predicted for a range of H and κ values. Then, the receiver functions are evaluated at the lag times predicted for each H, κ combination. At the correct choice of H, and κ, the three values will all have large amplitudes; stacking the values of all the phases for all the possible H, κ combinations will produce a maximum at the preferred crustal thickness and $\frac{V_P}{V_S}$ ratio. We perform both summation and multiplication stacks, which are shown in Figure 5. In the multiplication stacks, we set to zero the stack values for H-κ combinations that predict amplitudes opposite to those observed for the converted phases and their multiples. We assign identical weights to the Ps, PpPs, and PsPs + PpSs contributions, because we found

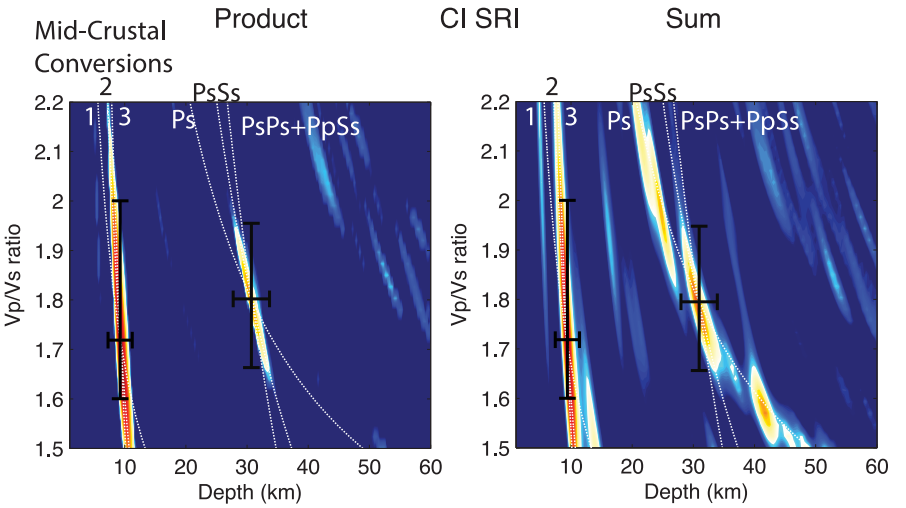

Figure 5. H-κ stacks of Ps receiver functions obtained by either multiplication (left) or summation (right) of the receiver functions evaluated at lag-times predicted for the Ps, PsSs, and PsPs+PpSs phases for each combination of H-κ. Large amplitudes in the stacks indicate values of thickness and Vp/Vs ratio that are most compatible with observed single-station Ps receiver functions. The black bars are uncertainty estimates, chosen to include the high-amplitude portion of the stack that is robust with respect to changes in reference Vp and relative weights of phases included in the stack. The dark blue is zero and warmer colors indicate larger amplitude signals. The numbers show the first midcrustal discontinuity (1) and its first two multiples (2,3).

that assigning different weights, as *Zhu and Kanamori* [2000] did in their study, produced little influence on our parameter selection. A search for optimal weights is possible, but would vary from station to station and is beyond the scope of this study. Incidentally, by using unweighted parameters, we highlight the significance of multiples compared to just the initial Ps phase, to which the most weight is typically assigned. The thickness of a layer and $\frac{Vp}{Vs}$ ratio estimates that we obtain depend weakly on the absolute compressional wave speed. For a reasonable range of average crustal V_P, this dependence introduces up to a $\pm$3 km uncertainty on our Moho depth estimates. Throughout this study, we used two values for average crustal compressional velocity in our H-κ stacks: 6.4 km/s as used by *Zhu and Kanamori* [2000], and 5.9 km/s as a lower-bound on reasonable average crustal V_P. We also quantify uncertainty on inferred H due to trade-offs between interface depth and $\frac{Vp}{Vs}$ ratio in the H-κ stacks. We do so by tabulating H values corresponding to the high and low $\frac{Vp}{Vs}$ ratios bracketing the high-amplitude portion of the H-κ stack, instead of only taking the values associated with the highest amplitude point of the stack. For most stations, the uncertainty due to $\frac{Vp}{Vs}$ ratio on H was 2 km, while for the ALBACORE data and very poor land stations, this uncertainty was as high as 8 km. We opted against pursuing more detailed quantitative treatments of uncertainty on H and $\frac{Vp}{Vs}$ from H-κ stacks, such as that used by *Zhu and Kanamori* [2000], because uncertainties obtained from these analyses tend to be far smaller than the ones we obtain from simple considerations described above (also see Table 3).

As a further way of quantitatively assessing the uncertainty of the Ps and Sp receiver functions, we carry out bootstrap analysis on Ps and Sp receiver function single-station stacks (see Supplementary Material of *Lekic et al.*, 2011 for more detail).

In this study, we seek to constrain the isotropic velocity structure of the lithosphere, and therefore do not attempt to constrain anisotropy by analyzing receiver function variation with back-azimuth. However, a number of investigators have documented strong lower-crustal anisotropy throughout Southern California [e.g., *Yan and Clayton*, 2007; *Porter et al.*, 2011]. At most of the coastal and ocean island stations, both Ps and Sp receiver function data span a broad range of back-azimuths (see Figure 3), and the presence of lower crustal anisotropy should not systematically bias the analysis of average receiver functions presented in this study. Nevertheless, anisotropy might manifest itself in more complicated receiver functions, with multiple or broad phases associated with intracrustal discontinuities and the Moho. On the other hand, for the ALBACORE stations, the back-azimuthal distribution of Ps and, particularly, Sp waveforms, is almost entirely restricted to three back-azimuths: the north-west, west, and south-east. In their systematic study of lower-crustal anisotropy across Southern California, *Porter et al.* [2011] find intermediate to weak anisotropy

Table 1. Average Moho Depth and Standard Deviation by Region IB = Inner Borderland, OB = Outer Borderland, AP = Abyssal Plain, WTR = Western Transverse Ranges, PR = Peninsular Ranges, and L.A. = Los Angeles Basin

	Moho Depth		Vp/Vs	
Region	Average	Std. Dev.	Average	Std. Dev.
IB	21.86	3.13	1.77	0.06
OB	28.17	4.16	1.75	0.05
AP	8.37	0.87	1.86	0.06
WTR	27.92	3.55	1.81	0.09
PR	32.54	4.04	1.77	0.06
L.A.	28.5	2.12	1.84	0.06

at CIA and SNCC the two offshore stations that they analyze. The trend of anisotropy at these stations is 216° and 150° (measured clockwise from North), respectively. If the first of these trends persists beneath the ALBACORE stations, then the north-western and south-eastern paths would be relatively unaffected by the anisotropy. If, instead, it is the second anisotropy trend that persists, then travel times along north-western and south-eastern paths would be affected by nearly opposite amounts. In either scenario, then, we would not expect ALBACORE results obtained by neglecting anisotropy to be strongly affected by lower crustal anisotropy, unless the strength and direction of anisotropy varies dramatically across the Continental Borderland.

3.3. Common-Conversion Point Stacks

To investigate the structure of the subcrustal lithosphere, we analyzed Sp receiver functions. Sp conversion points are displaced far from the receiver, so that different teleseismic source-receiver pairs sample different regions in the subsurface. To take advantage of multiply-sampled Sp conversion locales, we construct common-conversion point stacks. We begin by mapping Sp receiver functions calculated using the extended time multi taper implementation of *Lekic and Fischer* [2013] into the volume beneath our region of interest. We calculate the latitude, longitude, and depth corresponding to the lag times of the receiver function, by using ray tracing along the corresponding ray parameter and back azimuth through a depth profile of velocity constructed using the average crustal thickness and $\frac{Vp}{Vs}$ ratio (Table 1) and mantle velocities from ak135 [*Kennett et al*., 1995]. To obtain the value of the CCP stack at each point, we calculate a weighted average of nearby Sp receiver functions to mirror the decreasing resolution with depth (see *Lekic et al*. [2011] for more detail).

4. Results

4.1. Geographical Patterns in RFs

Qualitatively, we find that Ps receiver functions and the associated H-κ stacks and Moho/midcrustal phase maps among stations located on certain structural blocks are compellingly similar, while those on other blocks are strikingly dissimilar. For example, all stations located within the Los Angeles Basin have very similar Ps receiver functions, except for the two located on the western side of the Newport-Inglewood Fault. We will discuss this laterally abrupt transition in more detail in the Discussion section. Similarly, the Ps receiver function of station SNCC on San Nicolas Island in the Outer Borderland has much more in common with those at stations of the Peninsular Ranges than the much closer station CIA, located on Catalina Island in the Inner Borderland.

Since receiver functions are proxies for subsurface structure, they have direct implications for the structural evolution and potential deformation history of the region; therefore, it is important to undertake a more quantitative analysis. In order to objectively group receiver functions, we use cluster analysis, a method that quantifies the similarity between pairs of receiver functions and numerically verifies the patterns gleaned in our initial qualitative analysis. The usefulness of cluster analysis in identifying regions of similar structure from seismological constraints has recently been demonstrated using both upper mantle [*Lekic and Romanowicz*, 2011] and lower mantle [*Lekic et al*., 2012] shear wave speed profiles. Motivated by these studies, we apply cluster analysis to quantitatively and reproducibly identify similarities and differences of structures across the region. We use a MATLAB implementation of the hierarchical, agglomerative, method of cluster analysis.

Cluster analysis can be considered an objective means of grouping objects (in our case, Ps receiver function time series) in the sense that it uses a distance metric to quantify the (dis)similarity between objects. On the other hand, the choice of the distance metric is itself subjective, especially if it is chosen with a specific result in mind. Cognizant of this danger, we selected a distance metric that ignores geographic distance between stations, to avoid grouping of stations just because they were relatively close to one another.

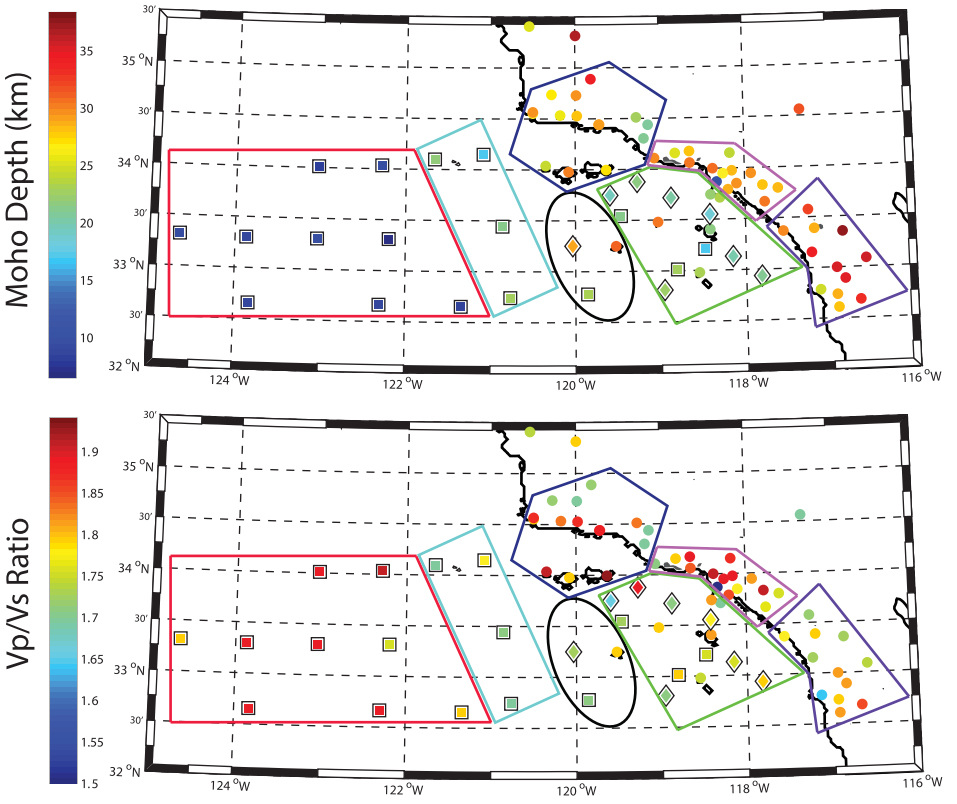

Figure 6. (top) Depths to the Moho for the ALBACORE (squares/diamonds) and island/coastal stations (circles) determined using H-κ stacking of Ps receiver functions. Note the systematic differences (relatively thin Inner Borderland, Outer Borderland, and coastal stations roughly equal, expected thickness for abyssal plain) in crustal thickness across different structural blocks. (bottom) $\frac{V_p}{V_s}$ ratios corresponding to the Moho depths (top) chosen from the H-κ stacks. Outlines encompass stations used in average and standard deviation calculations by region (Table 1). Red = abyssal plain stations, Light Blue = stations between the abyssal plain and Outer Borderland, Black = Outer Borderland stations, Dark Blue = Western Transverse Range stations, Pink = L.A. Basin stations, and Purple = Peninsular Ranges stations.

Instead, our distance metric equals one minus the correlation coefficient between two receiver functions, in order to identify which locations are characterized by most similar subreceiver structures. The distance between groups (clusters) of receiver functions is taken as the arithmetic mean of the distances between each pair of receiver functions across the two clusters.

Reassuringly, the pattern of stations identified through cluster analysis to have similar structure correspond to the groupings we inferred from qualitative considerations. Specifically, stations straddling different sides of the Newport-Inglewood Fault (near Long Beach, California) belong to different clusters, and stations SNCC (Outer Borderland), SBI (Island Block), are grouped together with stations in the Peninsular Ranges and station SRI (Western Transverse Range Block). We consider it unlikely that the observed similarities are due to event region (source) character as each receiver function is calculated from waveforms of several hundred earthquakes spanning different source regions (see Figure 3).

In addition to enabling us to identify regions with similar lithospheric structure, cluster analysis was useful in interpreting H-κ stacks that could not be unambiguously interpreted in isolation, such as those constructed at stations that had very poor quality data. In these cases, we used stations with similar receiver functions identified through cluster analysis to help guide our interpretations. This provided more confidence in our inferences of crustal structure parameters from the H-κ stacks, and helped ensure that our Moho (and midcrustal discontinuity) depths were consistently interpreted across stations. This is particularly important for our interpretations at station SNCC, which is detailed in the Discussion section.

4.2. Average Crustal Properties

H-κ stacking of Ps receiver functions yielded estimates of Moho depth and average crustal $\frac{Vp}{Vs}$ ratio at most stations in our data set. Figure 6 shows the maps of Moho depth (top) and average crustal $\frac{Vp}{Vs}$ ratio (bottom)

we obtained from H-κ analysis of Ps receiver functions. Some stations, such as those in the Los Angeles Basin, exhibited no clear Moho-related arrival that could be identified; we strongly suspect this is due to interference with multiples of the sedimentary piles present within the basin. At 13 stations, more than one choice of crustal parameters was compatible with the H-κ stacks. Since the duration of deployment, noise levels, and geologic setting varied widely between different stations, so did the reliability of the H-κ stacks, and, therefore, the inferences on crustal structure.

We find that the crustal thicknesses vary substantially across the region of study, from 6 to 8 km in the abyssal plain to >35 km beneath the Peninsular Ranges. We also find significant variations between average crustal thicknesses across adjacent structural blocks (see Table 1). Relatively thick crust is observed for the WTR block, as constrained by stations SCZ2, SMI, SRI, GATR, SBC, LGU, SDP, NJQ, SYP, WGR, STC, LCP, FIG, SMB, and MPP, which have an average Moho depth of 28.4 $\pm$ 3.9 km (1σ). Similar crustal thicknesses are obtained for the L.A. Basin, which has an average crustal thickness of 28.5 $\pm$ 2.1 km, and the Outer Borderland, whose three stations—SNCC and ocean bottom stations OBS06 and OBS26—have an average Moho depth of 28.2 $\pm$ 4.2 km. On the other hand, the Inner Borderland exhibits a substantially thinner crust, as constrained by stations CIA, FMP, RPV, SCI2, SBI, and ocean bottom stations OBS02, OBS03, and OBS27–OBS34, with an average Moho depth of 21.9 $\pm$ 3.2 km. The crust of the abyssal plain (OBS08–OBS21) appears to be unremarkable, with an average thickness of 8.4 $\pm$.9 km; it should be noted that much of the variation could be due to the lower quantity and quality of data. Interestingly, the Moho depth findings immediately west of the Patton Escarpment, constrained by OBS07, OBS22, OBS23, and OBS24, indicate that transition to shallow Moho depths typical of an oceanic tectonic setting takes place over a lateral distance of approximately 50 km. Thickest crust is found beneath the Peninsular Range, with stations (BCC, CAP, PLM, JCS, DPP, EML, SDR, BAR, OLP, SDG, GOR, SOF) having an average Moho depth of 32.5 $\pm$ 4.0 km, in agreement with previous studies [*Ichinose et al*., 1996; *Yan and Clayton*, 2007; *Ozakin and Ben-Zion*, 2014]. Stations that are not included in the average and standard deviation calculations (Table 1) are those with no clear Moho-related conversion: PHL, SMM, and OBS 07, 22, 23, and 24. Higher $\frac{Vp}{Vs}$ (> 1.8) ratios suggest the existence of a sedimentary or unconsolidated layer comprising the top of the crust, while typical values (1.6–1.8) indicate little to no sediment beneath the station.

At many of the L.A. Basin stations, we could not determine a Moho depth and $\frac{Vp}{Vs}$ ratio using H-κ stacking of Ps receiver functions because of contamination by multiples trapped by the sediment layer. Because Sp is not affected by multiples and sedimentary layers the way that Ps is, we often observe clear Moho-related conversion on Sp receiver functions for these stations. Stations LGU and SCZ2 in the Western Transverse Range block have two peaks in the H-κ stacks, either of which could be interpreted as the Moho, (LGU at 30.4 and 25.4 and SCZ2 at 27.4 and 20.4), but the deeper value has been chosen for both stations because the $\frac{Vp}{Vs}$ ratio associated with that choice seems more reasonable and these values coincide with the Moho depths found at surrounding stations. Other stations have alternate Moho choices, but this is typically because of poor data quality and/or contamination by multiples, and none of these stations have a double peak that looks like the one observed at SCZ2 and LGU. The possible Moho depths at LGU and SCZ2 differ by ~7 km, which has led to interpretations of their source being oceanic crust from the Monterey microplate [*Schmandt and Clayton*, 2013; *Nazareth and Clayton*, 2003; *Cheng*, 2008]. It is possible that one of these peaks is a multiple from a shallow midcrustal discontinuity, but this possibility seems unlikely at these two stations because of the large amplitude and deep but similar depths of the observed signals at these stations.

In addition to obtaining average crustal thicknesses and $\frac{Vp}{Vs}$ ratios, we also used H-κ stacking to characterize potential midcrustal discontinuities. Figure 7 and Table 2 show the depths and average $\frac{Vp}{Vs}$ associated with midcrustal discontinuities for stations at which they are observed. The first positive velocity increase was chosen at each land station because everything after it could (and typically was) a multiple of the first positive discontinuity. The estimates for $\frac{Vp}{Vs}$ ratios and uncertainty were given the broadest range that seemed reasonable because it is impossible to constrain the $\frac{Vp}{Vs}$ ratios to a narrow range using the H-κ stacks. In Table 2, the stations that are not included in the average and standard deviation calculations include stations with no midcrustal discontinuity: PHL, SMM, and ocean bottom stations OBS07, OBS23, and OBS24. Beneath the L.A. Basin, we find a generally consistent midcrustal discontinuity, with an average depth of 5.3 $\pm$1.6 km and an average $\frac{Vp}{Vs}$ ratio of 1.85. Beneath the Inner Borderland, Western Transverse Range block, and Peninsular Ranges, we observe the midcrustal discontinuity between 7 and 8 km depth, with $\frac{Vp}{Vs}$ ratios

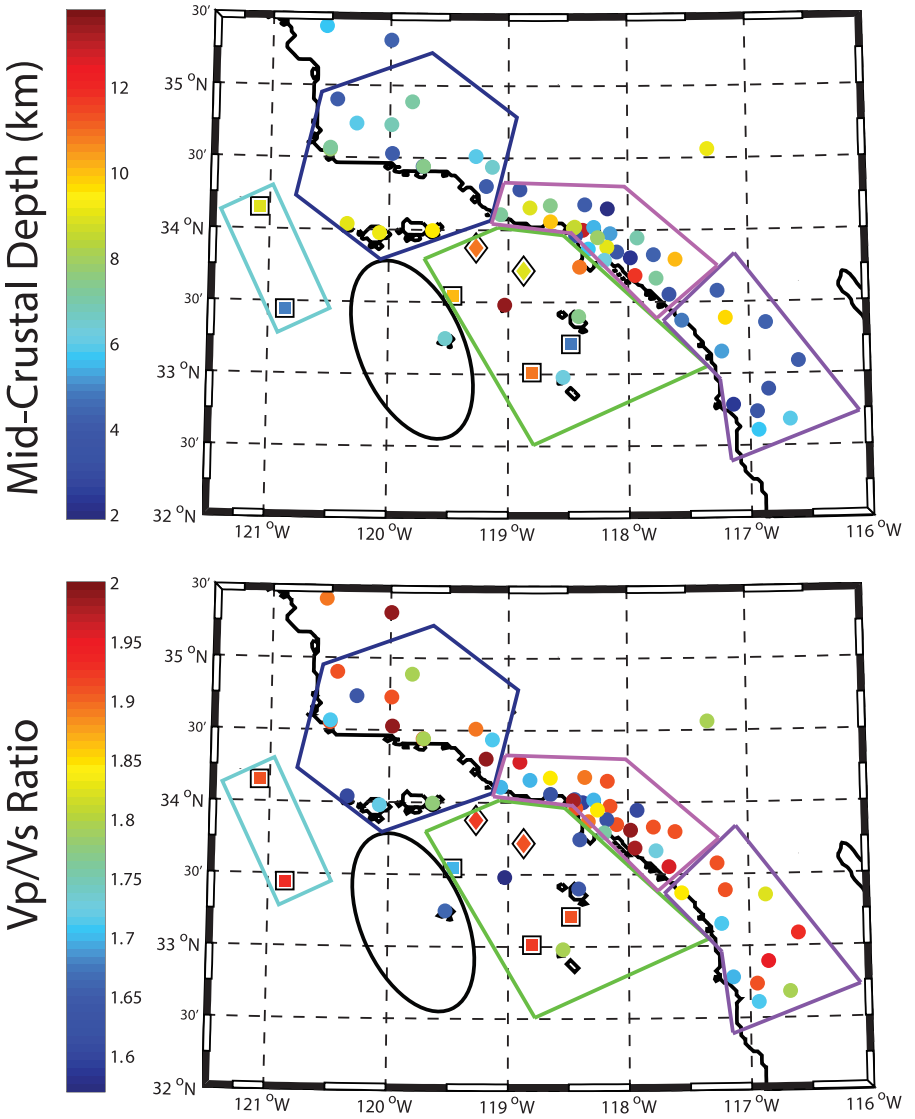

Figure 7. (top) Depths to the midcrustal layer for land/OBS stations determined using H-κ stacking of Ps receiver functions. Note the systematic differences between the L.A. Basin and the other regions. (bottom) $\frac{V_p}{V_s}$ ratios at stations corresponding to the midcrustal depths chosen (top) from the H-κ stacks. Shapes encompass stations used in average and standard deviation calculations by region. Light Blue- = stations between the abyssal plain and Outer Borderland, Black = Outer Borderland stations, Dark Blue = Western Transverse Range stations, Pink = L.A. Basin stations, and White = Peninsular Ranges stations.

$<$1.85. The Outer Borderland only has one station (SNCC) where the midcrustal discontinuity is observed, so there is no standard deviation or variance. At SNCC, the midcrustal discontinuity is observed at a depth of 6.6 km with a $\frac{Vp}{Vs}$ ratio of 1.66. There are no abyssal plain stations with midcrustal discontinuities except for two stations close to the Patton escarpment, which also have deep Mohos.

4.3. Sp Common-Conversion Point Stacks

Figure 8 shows vertical cross sections through our Sp CCP images, with warm (cool) colors indicating a rapid velocity increase (decrease) with depth. Slices C and D run in an east-west direction that is perpendicular to the coastline of southern California, and show lithospheric structure variations across the Continental Borderland. The Moho seen in these cross sections is consistent with the observations made from H-κ stacking. Cross sections A and B show a Moho at a depth of $\sim$20 km in the Inner Borderland and $\sim$30 km in the Western Transverse Range block (cross sections A and B) and L.A. Basin (cross section B). Cross section C shows a Moho at $\sim$30 km depth in the Outer Borderland, $\sim$20 km in the Inner Borderland and $\sim$30 km in the Peninsular Ranges. Cross section D shows the Moho transition between the abyssal plain and Western Transverse Range

Table 2. Average Midcrust Depth and Standard Deviation by Region IB = Inner Borderland, OB = Outer Borderland, WTR = Western Transverse Ranges, PR = Peninsular Ranges, and L.A. = Los Angeles Basin

	Mid-Crust		Vp/Vs	
Region	Average	Std. Dev.	Average	Std. Dev.
IB	7.83	3.09	1.78	0.12
OB	6.6	0	1.66	0
AP	N/A	N/A	N/A	N/A
WTR	6.99	2.21	1.78	0.12
PR	7.95	3.12	1.82	0.13
L.A.	5.3	1.57	1.85	0.13

block at about ~20 km depth and a depth of ~30 km in the Western Transverse Range block. These cross sections suggest an LAT that is roughly 70 km deep in the Peninsular Ranges, decreasing to 50 km depth in the Inner Borderland, and increasing back up to 80 km in the Outer Borderland. This is observable in the southern part (cross section C) of the Continental Borderland. Once the cross sections reach the Western Transverse Range block (fifth hash mark from the left of D and sixth hash mark from the top of A), the LAT depth appears to be constant at around 70–80 km depth. We find that the strength of the LAT signal in the cross sections weakens northward (cross section D), in agreement with recent findings of *Ford et al.* [2014].

We detect an unexpected positive phase in the southern part of the borderland that disappears as the cross sections move northward at ~50 km depth. This phase is present in the southern part (hash marks 1–4 of Figure 8) of cross section A, the most southern part (hash marks 1–2) of cross section B, and the western portion (hash marks 4–7) of cross section C. To assess the robustness of this phase—which indicates a velocity increase with depth at a depth of ~50 km—we constructed CCP stacks using different subsets of the data. We found that the phase exists in every subset of the data, even after removing each island station one at a time, or after removing all southern coastal stations (GOR, SDG, SOF). It is possible that this positive phase observed beneath the Outer Borderland is due to a fragment of trapped oceanic lithosphere that was partially subducted and then proceeded to translate with the overriding plate, but this interpretation is preliminary and warrants further investigation.

5. Discussion

5.1. Ocean Bottom Data Quality

A central aspect of this study was to obtain interpretable receiver functions from ocean bottom seismic data. Despite the relatively few usable waveforms gathered by stations of the ALBACORE deployment, we were able to obtain constraints on both crustal thickness variations—using Ps—and the depth to the lithosphere-asthenosphere transition—using Sp. At some stations, no robust estimates could be made based on the little available data. For example, OBS02 shows a Moho depth of 22.6 km in a receiver function created from five events, which is shown by bootstrap analysis to be insufficient to have confidence in the

Table 3. Comparison Our Crustal Thickness Estimates With Those From *Zhu and Kanamori* [2000] (Z&K), IRIS EARS, and *Porter et al.* [2011][a]

	This Study		Z&K	Z&K	IRIS	EARS	*Porter et al.* [2011]
Station	Moho	σ_H	Moho	σ_H	Moho	σ_H	Moho
BAR	33.7	2	34.2	1.6	40	2.4	N/A
CIA	21.9	2	22	1.7	24	1.1	22.7
FMP	23.6	2	N/A	N/A	24	1.0	21.0
JCS	36.3	3	34.9	1.3	36	1.6	N/A
MPP	34.8	1.5	N/A	N/A	31	1.4	33.9
PAS	24.4	6	28	1	25	1.2	30.5
PHL	25.6	2	24.3	1.1	24	0.2	26.4
PLM	38.3	5	34	0.8	29	1.2	N/A
PLS	28.9	1.5	28	0.7	N/A	N/A	N/A
RPV	22.3	1.5	21.5	0.7	20	0.3	27.1
SBC	29.8	2.5	33.3	1.5	28	5.3	N/A
SCI(2)	23.4	1.5	21.8	0.5	28	7.5	N/A
SNCC	31.5	3	21.1	0.9	32	8.1	22.3
TOV	25.6	3	N/A	N/A	25	1.9	35.7
VTV	32.4	1.5	30.9	0.9	32	1.7	30.6

[a]Where provided, error estimates are also specified as σ_H.

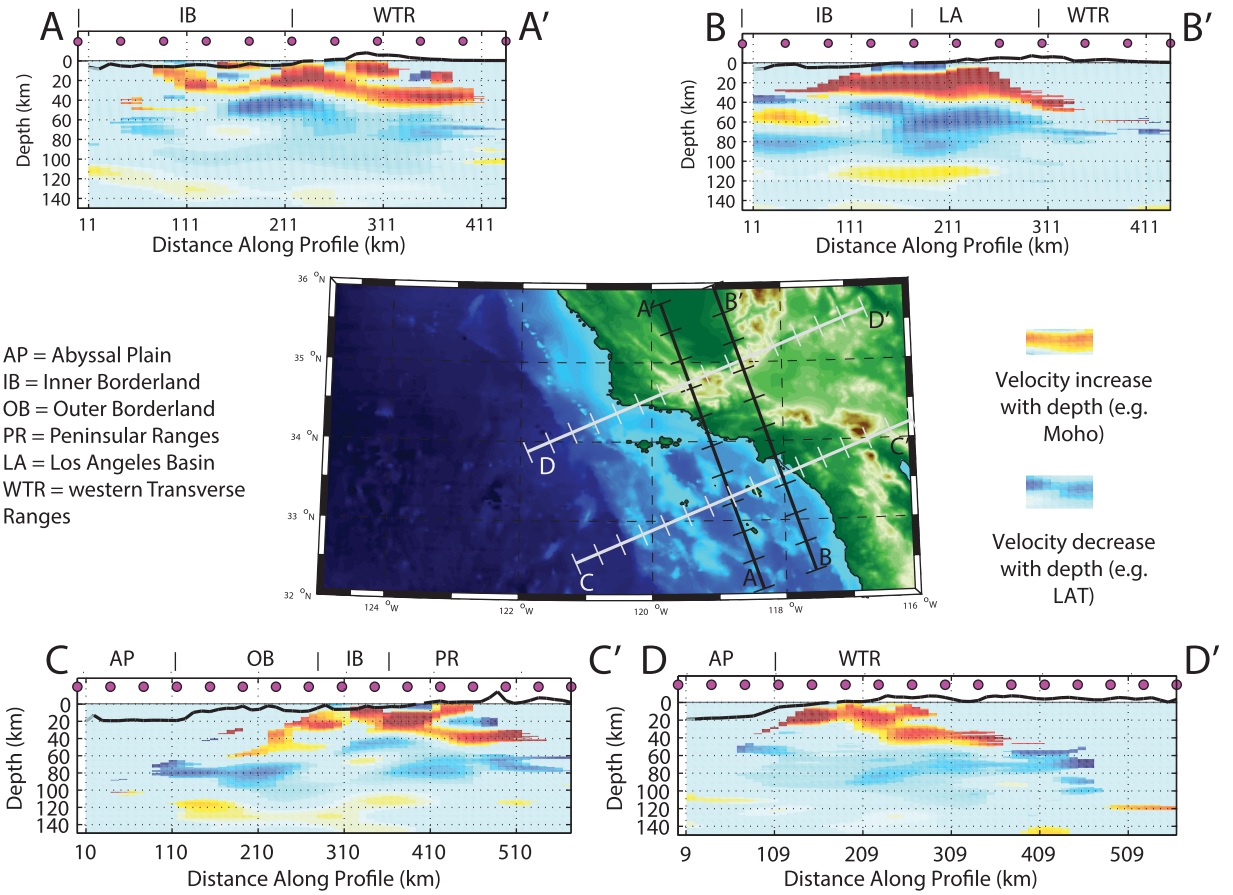

Figure 8. CCP stacks through cross sections. Red indicates a velocity increase with depth, while blue indicates a velocity decrease with depth. The colorscale saturates at 15% of the amplitude of the incoming S wave. The pink dots in the cross sections correlate to the black hash marks on the map. Note the changes in the strength of the lithospheric signal between the south and north in cross sections C and D, as well as the strong positive phase at 50 km depth in the western part of cross section C.

results. Caution must be taken when using the results at these stations to draw interpretations because of the small data set.

There are multiple reasons that ocean bottom data has higher noise levels relative to land station data. One reason is that the water layer above the seismometer allows for P waves to travel up through the water column and reflect off the ocean surface, traveling back down to the seismometer (i.e., water multiples). These water multiples typically arrive after the signal from the Moho, but before the LAT (although in some very shallow water stations it can arrive before the Moho signal as well). Another source of ocean-bottom noise is that the seismometers are often resting on soft, water-saturated sediments, which yield under pressure variations in the ocean environment, tilting the seismometers. Furthermore, ocean currents driven by tides are strong even on the abyssal plain, buffeting and tilting the ocean bottom seismometer. This tilting creates long-period noise of greater amplitude than is typically encountered at land stations, especially on the horizontal components, which are affected by the acceleration due to gravity as they are tilted away from horizontal. Another deleterious effect of the saturated sedimentary layer is that it traps seismic energy bouncing within it, overprinting signals from deeper structures such as the Moho and the LAT. Correcting for this effect can be difficult in practice, since the P wave velocity, the ratio of the P and S wave velocities, and the thickness of the sediment are all unknown. Finally, the traction exerted by the weight of the ocean above the seismometer changes the reflection and transmission coefficients across the sea floor, thereby affecting the estimation of the upgoing P-SV wavefields, which the receiver function method heavily relies on, because the common rotation methods [*Kennett*, 1991] assume that the surface has zero tractions.

In order to quantify the effects of thin sedimentary layers on the P and S waveforms, we simulated the effects of this sedimentary layer by calculating synthetic waveforms through a range of structures with

different sediment thicknesses using the SPECFEM2D code, which is capable of accurately modeling wave propagation through complex structures [*Komatitsch and Tromp*, 1999]. We generated synthetics with a variety of thicknesses for the sedimentary layer, ranging from .05 to 3 km, with an assumed V_p of 1.8 km/s and V_s of .3 m/s. The very high $\frac{Vp}{Vs}$ ratio is appropriate for water-saturated sediment. As anticipated, the synthetics show that when the sedimentary layer is thin, higher amplitude multiples from energy trapped in this layer arrived soon after the parent (P) wave. When the sedimentary layer was thicker, the amplitude of multiples decreased and their arrival was delayed, but the P-to-S conversions across the Moho and other features also arrived relatively later because of the increased $\frac{V_p}{V_s}$ ratio in the sedimentary layer. Therefore, both thick and thin overlying sedimentary layers complicate interpretation of Ps waveforms: (1) thin sediment does not cause a significant delay in the travel times of Moho P-to-S converted waves, but it overprints the sought-after signal by high-amplitude multiples, (2) thick sediment produces relatively weak multiples, but causes a significant delay in the travel times of converted phases. Furthermore, the synthetics demonstrate that shallow layer multiples affect the clarity of water multiples observations. This effect is seen in the data from abyssal plain stations, at which the sedimentary layer is not pronounced where the stations tend to have the clearest signatures of water multiples. Based on these synthetic analyses, we determined that the sedimentary layer particularly degrades signals at periods shorter than $\sim$8 s ($>$.125 Hz); therefore, we filter our data to longer periods using a fourth-order Butterworth filter with corner periods of .03 and .12 Hz. Similar filtering can be applied to other analyses of teleseismic converted waves recorded by ocean bottom stations because it reduces noise from the ocean environment, and avoids many of the complications due to the sedimentary layer, therefore making the use of OBS data more practical.

One adverse effect of filtering to long periods is that the resolution is degraded laterally, as well as dramatically in depth. In fact, since Ps lag-times for 7 km thick oceanic crust are $\sim$0.9 s, the very long-period bandpass renders the direct Ps converted across the oceanic Moho unobservable. Therefore, the crustal thickness constraints obtained in this study are derived from the H-κ stacks, which exploit later-arriving crustal multiples that, though smeared, remain observable. This can be seen in Figure 9, which shows H-κ stacks for station OBS28, located in the abyssal plain. Figure 9 (left and right plots) shows the product and sum stacks, on which the signal of the velocity jump across the oceanic Moho would appear as a distinct arrival near 6–8 km; exactly such a signal can easily be seen. However, the H-κ stacks of ALBACORE stations are contaminated by the water multiples, which manifest themselves as a booming negative signal in the stacks, visible in the middle plot of Figure 9. Due to its timing, the signal arising from the water multiples would obliterate those from velocity jumps in the 30–50 km depth range.

5.2. Crustal Thickness

Despite a scarcity of data, we were able to obtain crustal thickness estimates from Ps H-κ stacks throughout the study region. Though these results generally confirm previous inferences of crustal structure (Table 3), especially for the onshore regions, we note a number of consequential discrepancies between the current results and previous work. Previous Ps receiver function studies of this region to obtain crustal thickness include, among others, estimates by *Zhu and Kanamori* [2000], *Yan and Clayton* [2007], *Porter et al*. [2011], *Ozakin and Ben-Zion* [2014], and the IRIS EarthScope Automated Receiver Survey (IRIS EARS) program [*Crotwell and Owens*, 2005]. When comparing our findings, we focus our attention to coastal and island stations because they provide information on the structure—and therefore the formation and deformation—of the Continental Borderland.

Zhu and Kanamori [2000] and *Yan and Clayton* [2007] performed H-κ stacking of Ps receiver functions throughout the L.A. Basin, Peninsular Ranges, and Western Transverse Range block; however, along the coastline and in the off-shore region, they did not analyze many of the stations we were able to investigate in our study. There is relatively good agreement among the these several studies, consistently showing that crust gets thinner as it proceeds from the L.A. Basin and Peninsular Ranges into the Inner Borderland. In Table 3, we present crustal thickness estimates obtained for stations shared between our study, the *Zhu and Kanamori* [2000] and *Porter et al*. [2011]. Our crustal thickness estimates agree with both *Zhu and Kanamori* [2000] and *Porter et al*. [2011] at stations CIA, FMP, MPP, PHL and VTV, and agree with *Zhu and Kanamori* [2000] at JCS (which *Porter et al*. [2011] did not analyze). The fact that signal to noise ratios are highest at CIA, RPV, SCI(2), and VTV accounts for our agreement at these stations, as clear signals make for easily interpretable H-κ stacks. On the other hand, both of the other studies argue for significantly thinner crust at SNCC (21.1 and 22.3 versus 31.5 km), which we believe are due to misidentification of shallow crustal

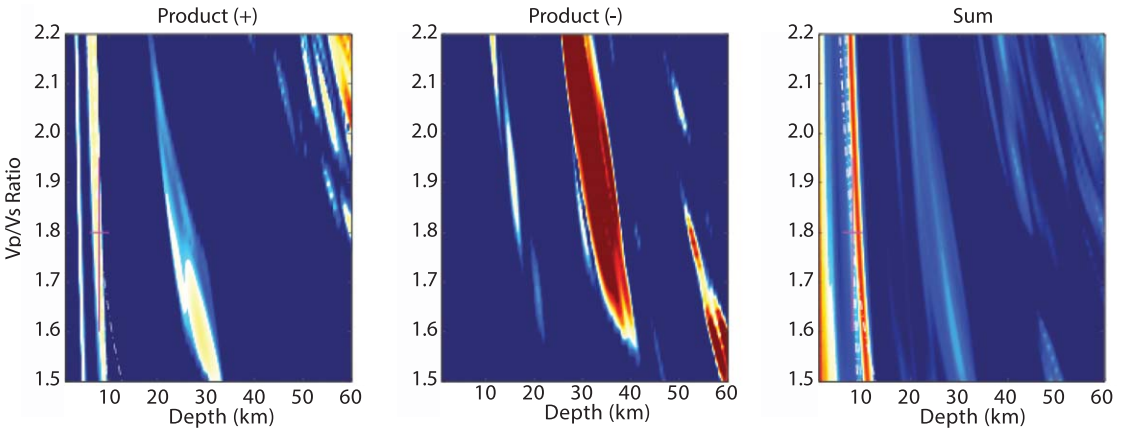

Figure 9. H-κ stacks for ALBACORE station OBS28, located in the abyssal plain. The left and right plots show the product and sum stacks, on which the signal of the velocity jump across the oceanic Moho would appear as a distinct arrival near 6–8 km; exactly such a signal can easily be seen. However, the H-κ stacks of ALBACORE stations are contaminated by the water multiples, which manifest themselves as a booming negative signal in the stacks (middle).

multiples. It should be noted that *Zhu and Kanamori* [2000]; *Porter et al*. [2011]; *Yan and Clayton* [2007] analyzed only three island stations, compared to the seven used in this study. At both RPV and TOV, *Porter et al*. [2011] find substantially thicker crust than us; the discrepancies may be due to the fact that both these stations appear to be underlain by very thick (8.6 and 9.6 km, respectively), highly anisotropic (20% and 18%, respectively), lower crustal layers, which *Porter et al*. [2011] constrain but we explicitly neglect in our analysis. Lower crustal anisotropy may also explain why our estimate of crustal thickness at PAS is a few kilometers thinner than estimates of *Zhu and Kanamori* [2000]; *Yan and Clayton* [2007]; and *Porter et al*. [2011].

IRIS EARS analyzed three of the island stations and some of the coastal stations, and the values it obtained at the three islands are comparable to the values we find in our study. IRIS EARS [*Crotwell and Owens*, 2005; *Trabant et al*., 2012] found similar (within 3 km) results for CIA, FMP, LGU, SBC, SNCC, and VTV even though it assumed a V_p of 6.048 km/s (instead of 6.4 km/s, which should make their estimates shallower than ours). However, IRIS EARS found a thicker crust under SCI2 (28 km, almost exactly the same as our alternative depth) and a significantly thicker (44 km) crust under SCZ2. The IRIS EARS values show generally similar continental crust along the coastline (LGU, FMP, SBC) that thins by ∼30% in the Inner Borderland and then thickens to values comparable to the coastline in the Outer Borderland.

It should also be noted that there is a relatively rapid change in crustal thickness between stations FMP/RPV and the L.A. Basin. Interestingly, this abrupt change agrees with previous analysis of two completely independent data sets, which argue for a rapid transition between the Inner Borderland and the L.A. Basin near the Newport-Inglewood Fault Zone [*Schmandt and Clayton*, 2013; *Nazareth and Clayton*, 2003]. In one study, high-density array data allowed *Schmandt and Clayton* [2013] to use teleseismic imaging to show a very sudden transition from the basin to the Inner Borderland structure accompanied by steeply dipping Moho (∼65°) at this boundary. *Nazareth and Clayton* [2003] used a continuous Pn phase to show that if the crust in the Inner Borderland is 22 km thick, which it appears to be in our study as well, the transition zone is constrained to initiate within a 2 km wide region beneath the southwest L.A. Basin, and has a width of 20–25 km.

The station SNCC was highly valuable in our analysis (see Figure 10) as it represents the only island station in the Outer Borderland, and provides the vast majority of the data for this structural block. The ALBACORE stations in this region that returned usable data (OBS06 and OBS26) had very high noise and not enough waveforms to allow high confidence interpretation. Therefore, reliability of SNCC H-κ stacks was crucial for quantifying differences between the crustal structure of this and surrounding blocks, and to understand the history of deformation in this region. In order to ensure that our conclusions were self-consistent and reproducible across different methods, we analyzed SNCC using Ps and Sp receiver functions, as well as Ps and Sp H-κ stacking.

Zhu and Kanamori [2000] concluded that the Moho in the Outer Borderland was at 21.1 ±.9 km depth, with a V_p of 6.4 km/s, and a $\frac{Vp}{Vs}$ ratio of 1.74. The results of IRIS EARS [*Crotwell and Owens*, 2005] changed during the course of our study, but as of March 2014, was reporting a Moho depth of 32 ± 8.1 km, with a Vp of

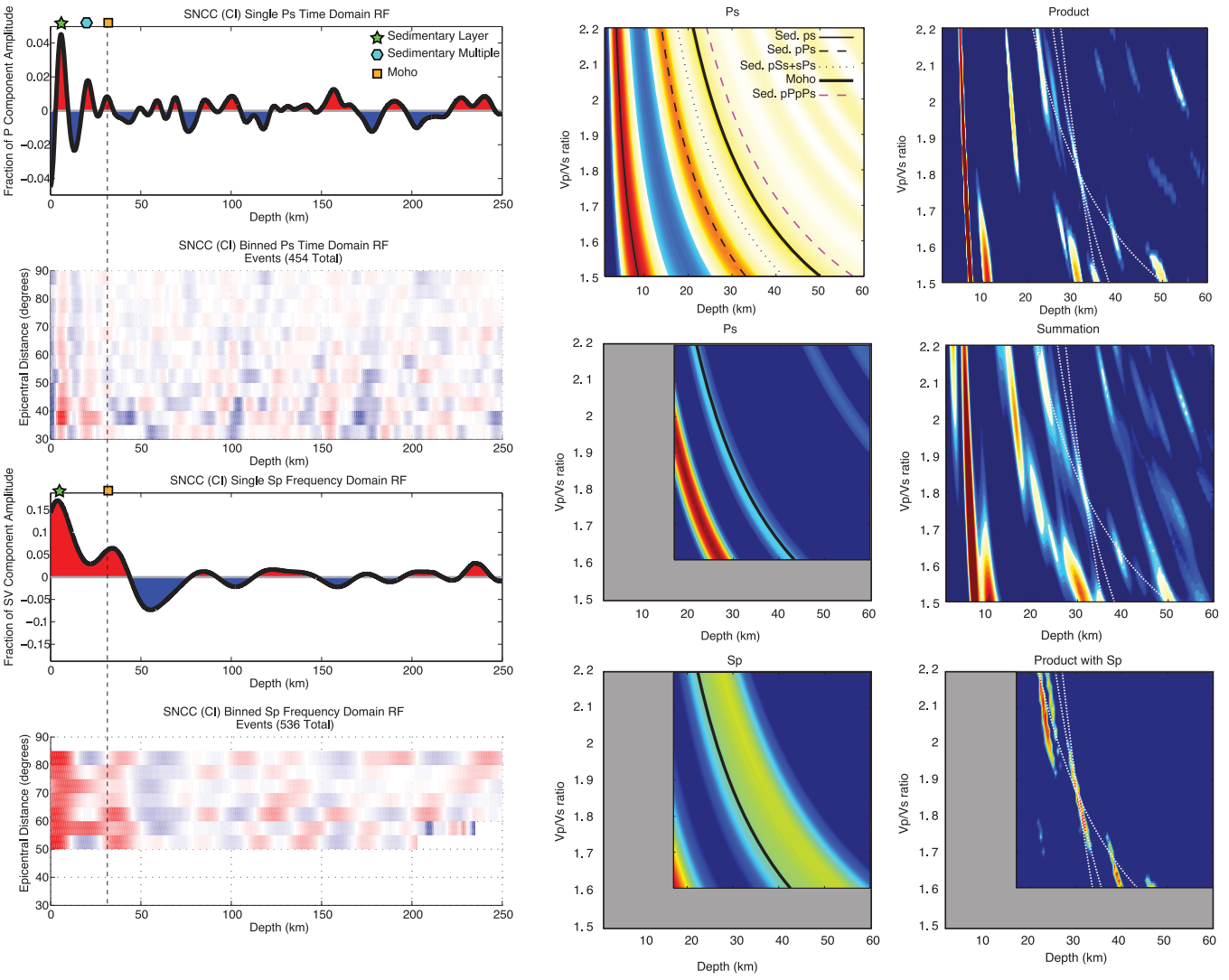

Figure 10. The left plots show the Ps and Sp receiver functions for SNCC, with the dashed line going through the Moho selection. The six plots on the right represent the H-κ stacking done for $\frac{Vp}{Vs}$ ratio and Moho constraints with an assumed Vp of 6.4 [*Zhu and Kanamori*, 2000] (top left) Ps with the sediment and multiples represented to show that the parameters selected in previous studies [*Zhu and Kanamori*, 2000] fall on the sedimentary multiple, adding to the strength of this phase, while the second Ps multiple arrives at the closely to our Moho, decreasing its amplitude. (middle and bottom left) An H-κ stack with Sp included in the stack (with range of H and κ reduced to avoid selection of sediment), so that the phase is consistent across all of the phases used for the H-κ stack and it can be clearly seen that the phase chosen (red phase) in previous studies [*Zhu and Kanamori*, 2000; *Porter et al.*, 2011] has no positive signal in the Sp stack. (top right) shows the product of the H-κ stack without the Sp phase taken into account. It should be noted that the parameters used in previous studies do not exist here. (middle right) the sum of the H-κ stack, which was the only method used previously and the previous parameters chosen do exist here. (bottom right) the product of the Sp H-κ stack, which shows that the phase chosen in this study is the only one that exists with reasonable parameters for a $\frac{Vp}{Vs}$ range and Moho depth.

6.048 km/s and a $\frac{Vp}{Vs}$ ratio of 1.6. *Porter et al*. [2011], on the other hand, find a two-layer, 22.3 km thick crust, whose lower layer shows 8.5% anisotropy. The crustal thickness preferred by *Zhu and Kanamori* [2000]; *Porter et al*. [2011] appears to be the best choice when first looking at the receiver functions and H-κ stacks for this station because they fall on a prominent peak in the Ps receiver function and the H-κ stack (see Figure 10). However, SNCC receiver functions unequivocally show a strong conversion (both Ps and Sp) at small lag times, consistent with a thin, shallow, upper crustal layer. When H-κ parameters are put in for this shallow, most likely sedimentary layer, it becomes apparent in the receiver functions and H-κ stacks that the first multiple from the midcrustal phase (the strongest positive phase) arrives at the same time as the direct conversion from the ostensible Moho at around 21 km depth (see Figure 10). Furthermore, the second multiple from the shallow layer arrives at the same lag time as the third positive phase. This second multiple (PpSs+PsPs) from the Ps conversion in the midcrustal layer will have a negative amplitude and therefore reduce the apparent amplitude of the positive third arrival, resulting in weak signal. Based on this analysis, we infer that the third positive arrival is the signal of the Moho beneath SNCC.

The H-κ product stacks (see Figure 10) do not appear to support the *Zhu and Kanamori* [2000] interpretation of SNCC stacks, since they lack a peak for their choice of crustal parameters. This absence implies that the sign of the Ps receiver function is opposite to that predicted for crustal multiples by their crustal thickness and Vp/Vs ratio. On the other hand, a small, but perceptible peak is present in both the sum and product H-κ stacks for our choice of crustal parameters. We further verified our results by analyzing the Sp receiver function, which is not affected by multiples from shallow structures, and should therefore highlight the true Moho. A clear positive phase is present in the Sp receiver function at a depth of $\sim$34 km, which is compatible with, though slightly deeper than our preferred Moho depth derived from the Ps H-κ stacks. The small discrepancy between the Sp and Ps results falls within our uncertainty estimate, and may be due to lower frequency content or higher noise levels of the Sp data. Indeed, when we incorporated Sp receiver function within the H-κ stacks, no peak was found to be present for a crustal thickness of 21 km. Instead, a clear peak is present for a crustal thickness of 30.0 km and a reasonable $\frac{Vp}{Vs}$ range (1.7–1.9), in agreement with the preferred crustal structure parameters.

Finally, we take advantage of the similarities among Ps receiver functions at other stations as yet another means of validating our interpretation of the SNCC signal. The pattern of three positive peaks with the third peak being the Moho or one large sedimentary peak and then another peak at a similar depth is prevalent in the Peninsular Range and southern coastal stations. Our cluster analysis also grouped SNCC with stations located along the Peninsular Ranges and southern coastline (as well as SBI). This correlation between receiver functions at SNCC and the stations of the Peninsular Ranges implies similarity of crustal structure and suggests that the Outer Borderland was translated and slightly rotated, as opposed to being rifted and thinned to compensate for the rotation of the Western Transverse Ranges because of the similarity in thickness. In this, our preferred interpretation, the varying thicknesses of the midcrustal layers between SNCC, the southern coastal and Peninsular Range stations can be explained by differences in original setting between mountainous, foothill, and coastal regions. Our use of multiple methods gives us additional confidence in these results. It is likely that substantial extension played a key role in the formation of the Continental Borderland because of the significant crustal thickness difference ($\sim$22 percent) between the Inner and Outer Borderland and the Inner Borderland and WTR block (Table 1). There is a $\sim$50 percent difference in thickness between the Peninsular Ranges and the Inner Borderland. These findings can be interpreted as supporting the *Crouch and Suppe* [1993] model for the formation of the Inner Borderland because this model relies heavily on extension and creation of a metamorphic core complex.

5.3. Midcrustal Discontinuity

At some, though not all stations, we observed a Ps conversion across a midcrustal discontinuity. The depth and average $\frac{Vp}{Vs}$ ratio associated with this discontinuity varies systematically across our region. As sedimentary basins tend to have higher $\frac{Vp}{Vs}$ ratios than most igneous rocks, we can use the maps in Figure 7 to determine which areas the midcrustal discontinuity is likely due to a sedimentary layer, and in which areas is it more likely a result of other structural or lithological interfaces. Additionally, the $\frac{Vp}{Vs}$ ratios of the midcrustal phase observed at stations in the L.A. Basin tend to be high ($>$1.85) and the average depth of the discontinuity observed here is $\sim$5.3 km (Table 2), we conclude that it occurs across the base of the sedimentary basin. Indeed, the average depth of the midcrustal phase yields a reasonable average thickness for the sedimentary layer in the L.A. Basin, considering that the maximum depth of the sediment is $\sim$10 km [*Yerkes et al*., 1965]. The depth and Vp/Vs ratios of midcrustal discontinuities detected at stations in surrounding areas and islands do not appear to be similar to the L.A. Basin because they generally have lower $\frac{Vp}{Vs}$ ratios ($<$1.85) and depths that range from 2 up to 13 km. This suggests that the discontinuity observed in the islands, Western Transverse Ranges, and Peninsular Ranges has a different origin than that beneath the L.A. Basin. This conclusion is supported by previous studies. For example, *Fuis et al*. [2003] observed a reflector in the upper crust at a depth of $\sim$3.5 km beneath the eastern portion of the WTR block, using Los Angeles Region Seismic Experiment 2 (LARSE-2) stations. They suggested that the reflector is caused by lithostatically pressured fluids in pores and cracks, which may be released during earthquakes. The midcrustal phase we observe in the same area (stations SMS, PDR, LCG, SMF2, and HLL) has a similar depth to this reflector (average of $\sim$3.3 km). Further west, *Namson and Davis* [1988] demonstrated that there is a fold system that has a detachment fault at a range of depths, which could be the origin of the large positive phase showing up in our receiver functions at stations WGR (7.2 km), SES (11.1 km), STC (8.8 km), MOP (13.2 km), and TOV (4.3 km).

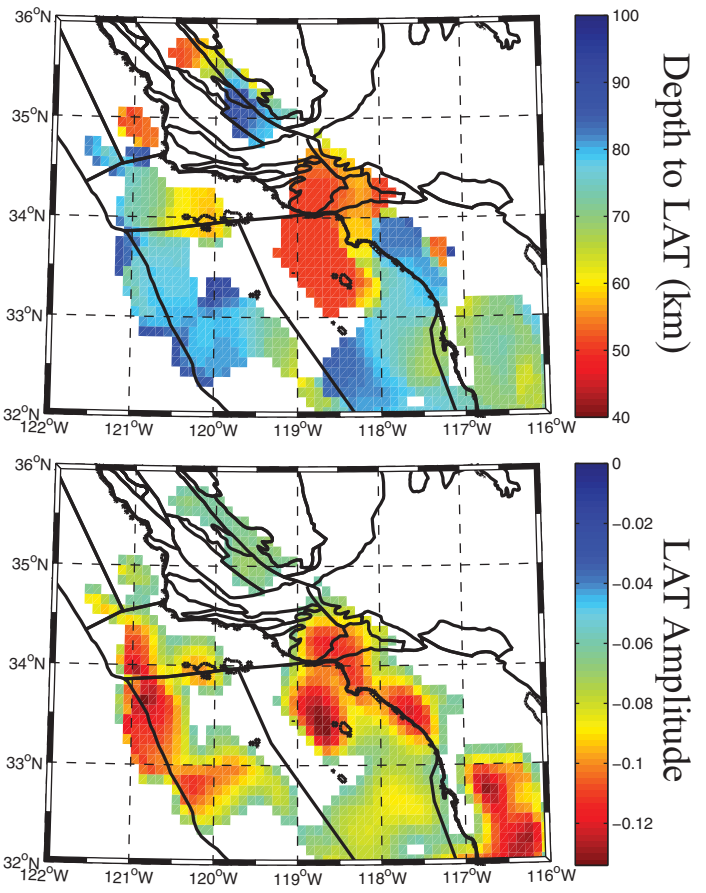

Figure 11. Maps showing depth to (top) and strength of the phase converted across (bottom) the lithosphere-asthenosphere transition (LAT), with warm colors indicating high amplitudes and shallow depths, and cool colors indicating weak amplitudes and deeper LAT depths. Areas with poor data coverage or that lacked a clear LAT-associated conversion in the Sp common-conversion point stacks are shown in white. Note that beneath both the Outer Borderland and the Peninsular Ranges (see Figure 1), the LAT-associated phase has a similar depth and amplitude, in stark contrast to that beneath the Inner Borderland.

Interestingly, we observe a mid-crustal phase at two of the three ALBACORE stations located in the abyssal plain but just west of the Patton Escarpment. The depth ($\sim$ 8) and $\frac{Vp}{Vs}$ ratios ($\sim$1.85) of these phases are consistent with oceanic crust, which may suggest that the deeper phase we identified as the Moho might result from underthrusting or more complex transition between oceanic and continental crusts. When considered in context with the observation of the $\sim$50 km deep, positive phase observed beneath the Outer Borderland (see Figure 8), this complex transition between oceanic and continental domains may be an updip expression of the same fragment of trapped oceanic lithosphere. Figure 12 illustrates this interpretation in a summary cartoon.

5.4. Lithosphere-Asthenosphere Transition

Variations in the depth to the LAT can also provide information on the structure and history of deformation in this region. *Lekic et al*. [2011] analyzed Sp receiver functions and performed common conversion point (CCP) stacking for data at almost all of the island stations that we use in this study in order to place constraints on LAT depth in the Inner and, to a lesser extent, the Outer Borderland. However, substantial gaps in data coverage prevented inferences on LAT structure in about half of the Inner Borderland, almost all of the Outer Borderland and some of the WTR block. Furthermore, no observations were made west of the Patton Escarpment, since those only became possible as a result of the ALBACORE deployment. The areas that they did cover show an Outer Borderland with similar thickness ($\sim$ 70 km) to the coastline and a relatively shallow LAT ($\sim$ 50 km) in the Inner Borderland. Our results, obtained with many additional waveforms from earthquakes that have occurred and stations that have been deployed since that study generally confirm the findings of *Lekic et al*. [2011], especially regarding the substantial lithospheric thinning beneath the Inner Borderland. However, we obtain a more detailed picture of structure beneath the Outer Borderland and confirm that the lithosphere of this block is very different, consistent with our interpretation based on crustal structure that the Outer Borderland has experienced a very different history of deformation. This can be seen in Figure 11, which documents the large variations in LAT depth across the region. The strength of the conversion across the LAT confirms that relatively strong conversions on the order of 10% of the incoming S wave are observed across the Continental Borderland, regardless of lithospheric thickness.

West of the Patton Escarpment, Sp data density is insufficient to enable CCP stacking, so instead, we analyze single-station Sp receiver functions. We find a clear, strong, negative phase, consistent with a velocity drop elsewhere interpreted as due to a seismic LAT, at ocean bottom stations 07, 08, 10, 11, 13, 15, 18, and 19.

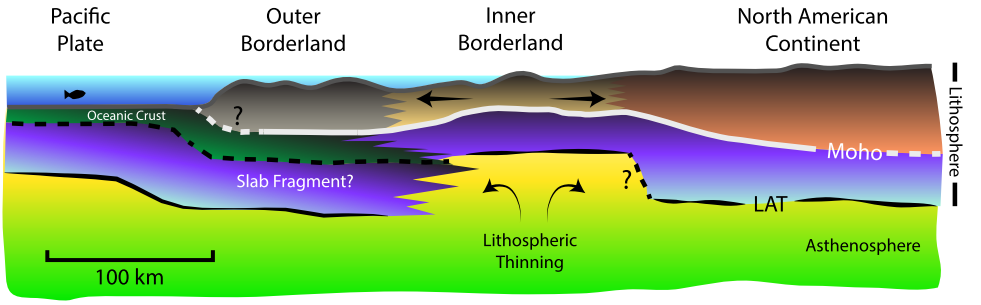

Figure 12. A possible interpretation of the borderland based on cross section C of Figure 8. The Inner Borderland has been formed from rifting and thinning of the lithosphere, while there is possibly a slab fragment of oceanic lithosphere that allowed the Outer Borderland and Western Transverse Range block to be translated/rotated without substantial thinning.

The depths of this phase, along with uncertainties estimated by bootstrapping, are shown in Table 4, along with the plate age from *Müller et al*. [2008]. The young age of the oceanic lithosphere in our region make our LAT depth estimates useful for determining its age-dependence. However, if the age and LAT depth for each individual station is considered in isolation, the relatively large uncertainties make it difficult to make any argument regarding how strongly the depth of the seismically observed LAT depends on age. This is because, within uncertainty, some of our stations fall on the LAT depths predicted by both an age-dependent model [e.g., *Kawakatsu et al*., 2009; *Kumar and Kawakatsu*, 2011], as well as models in which LAT depth is weakly dependent on age [e.g., *Evans et al*., 2005; *Karato*, 2012]. Nevertheless, by taking the mean age and depth of all stations in the abyssal plain (Table 4), and assuming that uncertainty on the LAT depth measurement at each station is independent of the others, we can reduce the uncertainty substantially. When we do this, we find that the average LAT depths are similar, within uncertainty, to those found beneath much older areas [e.g., *Schmerr*, 2012; *Kumar and Kawakatsu*, 2011], whereas age-dependent models predict a significantly thinner (∼30 %) lithosphere for our relatively young ages. Therefore, the inferred LAT depths that we obtain for stations in the Pacific abyssal plain are not at first glance compatible with predictions of models in which the depth of the seismically observable LAT depends strongly on age.

The similarity between the LAT depths we obtain and those found beneath older oceanic lithosphere is compatible with models in which dehydration controls the depth of the seismic LAT [e.g., *Evans et al*., 2005; *Olugboji et al*., 2013]. Though sited in somewhat older lithosphere, our findings are similar to those of *Evans et al*. [2005], who used images of the conductivity structure near the East Pacific Rise to argue that the oceanic lithosphere starts out ∼60 km thick, resulting from dehydration due to melting rather than age. Our results also appear compatible with a model in which the seismic LAT is due to anelastic effects resulting from elastically accommodated grain boundary sliding (EGBS) controlled by hydration [*Karato*, 2012]. While our results do not show evidence for a clear relationship between age and lithospheric thickness, it should be noted that this is a small sample size (eight stations) from a small range of ages. To have confidence in these results, which rely on the strong assumption that uncertainties in LAT depth determination across the abyssal plain stations are uncorrelated, more ocean bottom stations deployed over a wide range of ages are required.

Table 4. Estimates of Plate Age and Depth to the LAT for Select ALBACORE Stations[a]

Station	Age (Mya)	Depth (km)
OBS07	17.6	57 ± 20
OBS08	19.3	60 ± 13
OBS10	21.1	64 ± 15
OBS11	21.3	65 ± 15
OBS13	23.8	45 ± 17
OBS15	25.5	51 ± 16
OBS18	24.1	66 ± 17
OBS19	22.6	56 ± 15
Avg.	21.9 ± 2.6	58 ± 2.93

[a]Uncertainty on average LAT depth is calculated assuming uncorrelated errors on individual station estimates.

6. Conclusions

We have used observations of P-to-S and S-to-P conversions of teleseismic waves recorded at land (SCSN) and ocean-bottom (ALBACORE) three-component seismic stations to map variations in crustal and mantle lithosphere structure across the Continental Borderland. We show that by careful handpicking and judicious band-pass filtering of the ocean-bottom data, we are able to obtain interpretable receiver

functions. Using cluster analysis, we quantitatively show that the receiver functions bear evidence of similarities within and differences among the main structural blocks. Using H-κ stacking, we obtain estimates of crustal thickness and average V_P/V_S variations throughout the region. Using CCP stacking of Sp receiver functions, we have also constrained variations in the depth to the seismic lithosphere-asthenosphere transition (LAT) across the region.

At many stations across the region, we detect a pronounced conversion across a midcrustal discontinuity; the origin of this phase is sometimes due to the base of a sedimentary layer, and at other times appears to indicate a deeper lithological contrast. Our main observations are schematically illustrated in Figure 12. We find that the crustal and lithospheric thickness beneath the Outer Borderland is similar to that of the onshore regions, consistent with a history of deformation dominated by translation. In stark contrast, we confirm the presence of substantially thinned crust and lithosphere beneath the Inner Borderland, consistent with a deformation history involving substantial extension. Crustal thickness estimates obtained using ALBACORE data immediately west of the Patton Escarpment indicate that transition to shallow Moho depths typical of an oceanic tectonic setting takes place over a lateral distance of approximately 50 km, providing a unique constraint on the nature of the transition from oceanic-type to continental-type crust. We also observe anomalous crustal structure in the vicinity of the Patton Escarpment, which we interpret together with the observation of a persistent positive Sp conversion consistent with a velocity jump with depth in common conversion point stacks at ~50 km, as evidence of a lithospheric fragment beneath the Outer Borderland. This fragment is also illustrated in Figure 12, and we suggest that it may have allowed the Outer Borderland and Western Transverse Range block to be translated/rotated without substantial thinning experienced in the Inner Borderland region. Finally, our estimates of the depth to the seismic LAT beneath the Pacific plate do not appear to show evidence for substantial age-dependence of the depth to the seismic LAT, constraining models of the nature of the LAT.

Acknowledgments

Seismic data used in this work are freely accessible from the IRIS Data Management Center. Codes and data products besides those explicitly listed in the manuscript are available from the corresponding author. This work was supported in part by National Science Foundation grant EAR-1352214 to V. Lekic. ALBACORE was made possible with instruments and logistical support of the U.S. National Ocean Bottom Seismic Instrumentation Pool (OBSIP) at Scripps Institute of Oceanography; in particular, thanks go to Jeff Babcock, Ernie Aaron, Phil Thai, and Mark Gibaud. The deployment and recovery cruises were made possible with the equipment and logistical support of the University-National Oceanographic Laboratory System (UNOLS) vessel fleet and staff support at Scripps with particular thanks to Jon Meyer, Brian Rowe, and Meghan Donohue. M. Kohler and D. Weeraratne thank Captain Curl and the crew of R/V Melville for assistance during the 2010 OBS deployment cruise, and Captain Vullo and the crew of R/V New Horizon during the 2011 OBS recovery cruise. This work was supported by the National Science Foundation (grant OCE-0825254). We thank 3 anonymous reviewers for thoughtful and constructive comments that yielded a much improved manuscript.

References

Abt, D. L., K. M. Fischer, S. W. French, H. A. Ford, H. Yuan, and B. Romanowicz (2010), North American lithospheric discontinuity structure imaged by Ps and Sp receiver functions, *J. Geophys. Res.*, *115*, B09301, doi:10.1029/2009JB006914.

Ammon, C. J., T. Lay, H. Kanamori, and M. Cleveland (2011), A rupture model of the 2011 off the Pacific coast of Tohoku earthquake, *Earth Planets Space*, *63*(7), 693–696.

Atwater, T., and J. Stock (1998), Pacific-North America plate tectonics of the Neogene southwestern United States: An update, *Int. Geol. Rev.*, *40*(5), 375–402.

Bohannon, R. G., and E. Geist (1998), Upper crustal structure and Neogene tectonic development of the California continental borderland, *Geol. Soc. Am. Bull.*, *110*(6), 779–800.

Bostock, M. (1998), Mantle stratigraphy and evolution of the Slave province, *J. Geophys. Res.*, *103*(B9), 21,183–21,200.

Carter, J. N., B. P. Luyendyk, and R. R. Terres (1987), Neogene clockwise tectonic rotation of the eastern Transverse Ranges, California, suggested by paleomagnetic vectors, *Geol. Soc. Am. Bull.*, *98*(2), 199–206.

Cheng, J. C. (2008), Seismic evidence and tectonic significance of an intracrustal reflector beneath the inner California Continental Borderland and Peninsular ranges, MS thesis, Univ. of Texas, El Paso.

Crotwell, H. P., and T. J. Owens (2005), Automated receiver function processing, *Seismol. Res. Lett.*, *76*(6), 702–709.

Crouch, J. K. (1979), Neogene tectonic evolution of the California Continental Borderland and western Transverse Ranges, *Geol. Soc. Am. Bull.*, *90*(4), 338–345.

Crouch, J. K., and J. Suppe (1993), Late cenozoic tectonic evolution of the Los Angeles basin and inner California borderland: A model for core complex-like crustal extension, *Geol. Soc. Am. Bull.*, *105*(11), 1415–1434.

Evans, R. L., G. Hirth, K. Baba, D. Forsyth, A. Chave, and R. Mackie (2005), Geophysical evidence from the MELT area for compositional controls on oceanic plates, *Nature*, *437*(7056), 249–252.

Ford, H. A., K. M. Fischer, and V. Lekic (2014), Localized shear in the deep lithosphere beneath the San Andreas fault system, *Geology*, *42*(4), 295–298.

Fuis, G. S., et al. (2003), Fault systems of the 1971 San Fernando and 1994 Northridge earthquakes, Southern California: Relocated aftershocks and seismic images from LARSE II, *Geology*, *31*(2), 171–174.

Grove, M., G. Bebout, C. Jacobson, A. Barth, D. Kimbrough, R. King, H. Zou, O. Lovera, B. Mahoney, and G. Gehrels (2008), The Catalina Schist: Evidence for middle Cretaceous subduction erosion of southwestern North America, in Formation and applications of the sedimentary record in arc collision zones, Special Publication, *Geol. Soc. Am. Spec. Pap. 436*, edited by A. E. Draut, P. D. Clift, and D. W. Scholl, pp. 335–361, Geol. Soc. of Am., Boulder, Colo.

Helffrich, G. (2006), Extended-time multitaper frequency domain cross-correlation receiver-function estimation, *Bull. Seismol. Soc. Am.*, *96*(1), 344–347.

Howell, D., H. McLean, and J. Vedder (1976), Cenozoic tectonism on Santa Cruz Island, in Aspects of the Geologic History of the California Borderland, edited by D. G. Howell, *Am. Assoc. Pet. Geol. Pac. Sect., Misc. Publ.*, *24*, 392–416.

Ichinose, G., S. Day, H. Magistrale, T. Prush, F. Vernon, and A. Edelman (1996), Crustal thickness variations beneath the Peninsular Ranges, southern California, *Geophys. Res. Lett.*, *23*(22), 3095–3098.

Junger, A. (1976), Offshore structure between Santa Cruz and Santa Rosa Islands, in Aspects of the Geologic History of the California Borderland, edited by D. G. Howell, *Am. Assoc. Pet. Geol. Pac. Sect. Misc. Publ.*, *24*, 418–426.

Kamerling, M. J., and B. P. Luyendyk (1979), Tectonic rotations of the Santa Monica Mountains region, western Transverse Ranges, California, suggested by paleomagnetic vectors, *Geol. Soc. Am. Bull.*, *90*(4), 331–337.
Karato, S. (2012), On the origin of the asthenosphere, *Earth Planet. Sci. Lett.*, *321*, 95–103.
Kawakatsu, H., P. Kumar, Y. Takei, M. Shinohara, T. Kanazawa, E. Araki, and K. Suyehiro (2009), Seismic evidence for sharp lithosphere-asthenosphere boundaries of oceanic plates, *Science*, *324*(5926), 499–502.
Kennett, B. (1991), The removal of free surface interactions from three-component seismograms, *Geophys. J. Int.*, *104*(1), 153–163.
Kennett, B., E. Engdahl, and R. Buland (1995), Constraints on seismic velocities in the Earth from traveltimes, *Geophys. J. Int.*, *122*(1), 108–124.
Kohler, M. D., and Science Party (2010), ALBACORE OBS Deployment Cruise Report. [Available at http://kohler.caltech.edu/ALBACORE/ALBACORE_2010_Cruise_Report.pdf.]
Kohler, M. D., and Science Party (2011), ALBACORE OBS Recovery Cruise Report. [Available at http://kohler.caltech.edu/ALBACORE/ALBACORE_2011_Cruise_Report.pdf.]
Kolb, J., and V. Lekic (2014), Receiver function deconvolution using transdimensional hierarchichal Bayesian inference, *Geophys. J. Int.*, *197*(3), 1719–1735.
Komatitsch, D., and J. Tromp (1999), Introduction to the spectral element method for three-dimensional seismic wave propagation, *Geophys. J. Int.*, *139*(3), 806–822.
Kumar, P., and H. Kawakatsu (2011), Imaging the seismic lithosphere-asthenosphere boundary of the oceanic plate, *Geochem. Geophys. Geosyst.*, *12*, Q01006, doi:10.1029/2010GC003358.
Langston, C. A. (1977), Corvallis, Oregon, crustal and upper mantle receiver structure from teleseismic P and S waves, *Bull. Seismol. Soc. Am.*, *67*(3), 713–724.
Lekic, V., and K. Fischer (2013), Contrasting lithospheric signatures across the western United States revealed by Sp receiver functions, *Earth Planet. Sci. Lett.*, *402*, 90–98 doi:10.1016/j.epsl.2013.11.026.
Lekic, V., and B. Romanowicz (2011), Tectonic regionalization without a priori information: A cluster analysis of upper mantle tomography, *Earth Planet. Sci. Lett.*, *308*(1), 151–160.
Lekic, V., S. W. French, and K. M. Fischer (2011), Lithospheric thinning beneath rifted regions of southern California, *Science*, *334*(6057), 783–787.
Lekic, V., S. Cottaar, A. Dziewonski, and B. Romanowicz (2012), Cluster analysis of global lower mantle tomography: A new class of structure and implications for chemical heterogeneity, *Earth Planet. Sci. Lett.*, *357*, 68–77.
Ligorría, J. P., and C. J. Ammon (1999), Iterative deconvolution and receiver-function estimation, *Bull. Seismol. Soc. Am.*, *89*(5), 1395–1400.
Luyendyk, B. P. (1991), A model for Neogene crustal rotations, transtension, and transpression in southern California, *Geol. Soc. Am. Bull.*, *103*(11), 1528–1536.
Luyendyk, B. P., M. J. Kamerling, and R. Terres (1980), Geometric model for Neogene crustal rotations in southern California, *Geol. Soc. Am. Bull.*, *91*(4), 211–217.
McQuarrie, N., and B. P. Wernicke (2005), An animated tectonic reconstruction of southwestern North America since 36 Ma, *Geosphere*, *1*(3), 147–172.
Müller, R. D., M. Sdrolias, C. Gaina, and W. R. Roest (2008), Age, spreading rates, and spreading asymmetry of the world's ocean crust, *Geochem. Geophys. Geosyst.*, *9*, Q04006, doi:10.1029/2007GC001743.
Namson, J., and T. Davis (1988), Structural transect of the western Transverse Ranges, California: Implications for lithospheric kinematics and seismic risk evaluation, *Geology*, *16*(8), 675–679.
Nazareth, J. J., and R. W. Clayton (2003), Crustal structure of the Borderland-Continent Transition Zone of southern California adjacent to Los Angeles, *J. Geophys. Res.*, *108*(B8), 2404, doi: 10.1029/2001JB000223.
Nicholson, C., C. C. Sorlien, T. Atwater, J. C. Crowell, and B. P. Luyendyk (1994), Microplate capture, rotation of the western Transverse Ranges, and initiation of the San Andreas transform as a low-angle fault system, *Geology*, *22*(6), 491–495.
Olugboji, T. M., S. Karato, and J. Park (2013), Structures of the oceanic lithosphere-asthenosphere boundary: Mineral-physics modeling and seismological signatures, *Geochem. Geophys. Geosyst.*, *14*, 880–901, doi:10.1002/ggge.20086.
Ozakin, Y., and Y. Ben-Zion (2014), Systematic receiver function analysis of the Moho geometry in the Southern California Plate-Boundary region, *Pure Appl. Geophys.*, 1–18, doi:10.1007/s00024-014-0924-6.
Porter, R., G. Zandt, and N. McQuarrie (2011), Pervasive lower-crustal seismic anisotropy in Southern California: Evidence for underplated schists and active tectonics, *Lithosphere*, *3*, 201–220, doi:10.1130/L126.1.
Schmandt, B., and R. W. Clayton (2013), Analysis of teleseismic P waves with a 5200-station array in Long Beach, California: Evidence for an abrupt boundary to Inner Borderland rifting, *J. Geophys. Res.*, *118*, 5320–5338, doi:10.1002/jgrb.50370.
Schmerr, N. (2012), The Gutenberg discontinuity: Melt at the lithosphere-asthenosphere boundary, *Science*, *335*(6075), 1480–1483.
ten Brink, U. S., J. Zhang, T. M. Brocher, D. A. Okaya, K. D. Klitgord, and G. S. Fuis (2000), Geophysical evidence for the evolution of the California Inner Continental Borderland as a metamorphic core complex, *J. Geophys. Res.*, *105*(B3), 5835–5857.
Trabant, C., A. R. Hutko, M. Bahavar, R. Karstens, T. Ahern and R. Aster (2012), Data products at the IRIS DMC: Stepping-stones for research and other application, *Seismol. Res. Lett.*, *83*(6), 846–854, doi:10.1785/0220120032.
Wilson, D. C., D. Angus, J. F. Ni, and S. P. Grand (2006), Constraints on the interpretation of S-to-P receiver functions, *Geophys. J. Int.*, *165*(3), 969–980.
Yan, Z., and R. W. Clayton (2007), Regional mapping of the crustal structure in southern California from receiver functions, *J. Geophys. Res.*, *112*, B05311, doi:10.1029/2006JB004622.
Yerkes, R. F., T. McCulloh, J. Schoellhamer, and J. G. Vedder (1965), Geology of the Los Angeles basin, California: An introduction, *U.S. Geol. Surv. Prof. Pap. 420*, A1–A57.
Zhu, L., and H. Kanamori (2000), Moho depth variation in southern California from teleseismic receiver functions, *J. Geophys. Res.*, *105*(B2), 2969–2980.